RETI-DIFF: ILLUMINATION DEGRADATION IMAGE RESTORATION WITH RETINEX-BASED LATENT DIFFUSION MODEL

Anonymous authors
Paper under double-blind review

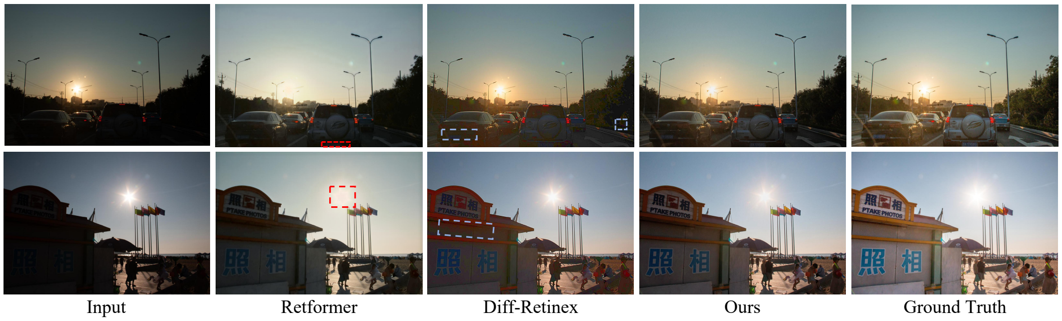

Figure 1: Results of Retinex-based cutting-edge image restoration methods, where our Reti-Diff can better highlight details and correct color distortions. The dashed boxes indicate failure cases or artifacts produced by existing methods, which can be properly addressed by our approach.

ABSTRACT

Illumination degradation image restoration (IDIR) techniques aim to improve the visibility of degraded images and mitigate the adverse effects of deteriorated illumination. Among these algorithms, diffusion models (DM) have shown promising performance but are often burdened by heavy computational demands and pixel misalignment issues when predicting the image-level distribution. To tackle these problems, we propose to leverage DM within a compact latent space to generate concise guidance priors and introduce a novel solution called Reti-Diff for the IDIR task. Specifically, Reti-Diff comprises two significant components: the Retinex-based latent DM (RLDM) and the Retinex-guided transformer (RGformer). RLDM is designed to acquire Retinex knowledge, extracting reflectance and illumination priors to facilitate detailed reconstruction and illumination correction. RGformer subsequently utilizes these compact priors to guide the decomposition of image features into their respective reflectance and illumination components. Following this, RGformer further enhances and consolidates these decomposed features, resulting in the production of refined images with consistent content and robustness to handle complex degradation scenarios. Extensive experiments demonstrate that Reti-Diff outperforms existing methods on three IDIR tasks, as well as downstream applications. [1]

1 INTRODUCTION

Illumination degradation image restoration (IDIR) seeks to enhance the visibility and contrast of degraded images while mitigating the adverse effects of deteriorated illumination, *e.g.*, indefinite noise and variable color deviation. IDIR has been investigated in various domains, including low-light image enhancement (Cai et al., 2023), underwater image enhancement (Guo et al., 2023), and backlit image enhancement (Liang et al., 2023). By addressing illumination degradation, the enhanced images are expected to exhibit improved visual quality, making them more suitable for decision-making or subsequent tasks like nighttime object detection and segmentation.

Traditional IDIR approaches (Fu et al., 2016; Ueng & Scharf, 1995) primarily rely on manually crafted enhancement techniques with limited generalization capabilities. Leveraging the robust

[1] The source code will be made publicly available.

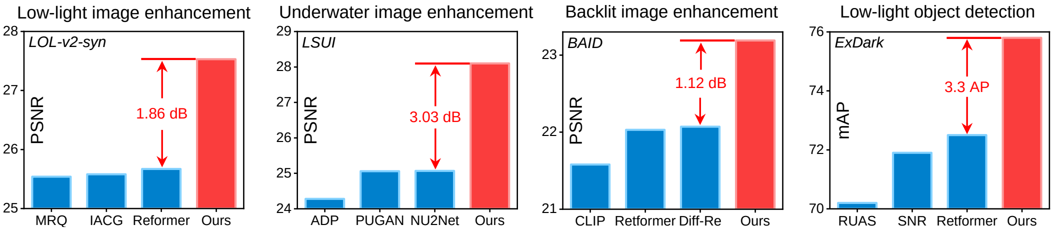

Figure 2: Our Reti-Diff achieves a leading place in three IDIR tasks and the low-light object detection task, and outperforms the corresponding cutting-edge techniques on these tasks, where CLIP and Diff-Re are short for CLIP-LIT (Liang et al., 2023), Diff-Retinex (Yi et al., 2023).

feature extraction capabilities of convolutional neural networks and transformers, a series of deep learning-based methods (Cai et al., 2023; Jiang et al., 2021) have been proposed and have achieved remarkable success in the IDIR domain. However, as depicted in Figs. 1 and 2, they still face challenges in complex illumination degradation scenarios due to their constrained restoration capacity.

To overcome this, deep generative models, like generative adversarial networks (He et al., 2023a), have gained popularity for their generative abilities. Recently, the diffusion model (DM) (Yi et al., 2023) has been introduced to the IDIR field for high-quality image restoration. However, existing DM-based methods, *e.g.*, Diff-Retinex (Yi et al., 2023) and GSAD (Jinhui et al., 2023), apply DM directly to image-level generation, leading to two main challenges: **(1)** These methods incur high computational costs, as predicting the image-level distribution requires a large number of inference steps. **(2)** The enhanced results may exhibit pixel misalignment with the original clean image in terms of restored details and local consistency. For example, as shown in Fig. 1, Diff-Retinex fails to recover the car's details in the top row and introduces severe artifacts in the bottom row.

To address the above challenges, we introduce a latent diffusion model (LDM) to solve the IDIR problem. The computational burden is reduced by applying DM in the low-dimensional, compact latent space. In addition, by integrating LDM with transformers, we prevent pixel misalignment in generated images (see Fig. 1), a common issue in deep generative models. Unlike existing LDM-based methods that rely solely on priors extracted from the RGB domain, our method, tailored to the specific characteristics of IDIR tasks, empowers LDMs to extract Retinex information from both the reflectance and illumination domains. This adaptation allows our method to generate high-fidelity Retinex priors directly from low-quality input images. The compact priors preserve high-quality information while minimizing the impact of degradation. Thus, our method simultaneously enhances image details using the reflectance prior and corrects color distortions with the illumination prior, resulting in visually appealing images with favorable downstream tasks.

With this inspiration, we present Reti-Diff, the first LDM-based solution to tackle the IDIR problem. Reti-Diff, depicted in Fig. 3, consists of two primary components: the Retinex-based LDM (RLDM) and the Retinex-guided transformer (RGformer). Initially, RLDM is employed to generate Retinex priors, which are then integrated into RGformer to produce visually appealing results. To ensure the generation of high-quality priors, we propose a two-phase training approach, wherein Reti-Diff undergoes initial pretraining followed by subsequent RLDM optimization. **In phase I**, we introduce a Retinex prior extraction (RPE) module to compress the ground-truth image into the highly compact Retinex priors, namely the reflectance prior and the illumination prior. These priors are then sent to RGformer to guide feature decomposition and the generation of reflectance and illumination features. Afterward, RGformer employs the Retinex-guided multi-head cross attention (RG-MCA) and dynamic feature aggregation (DFA) module to refine and aggregate the decomposed features, ultimately producing enhanced images with coherent content and ensuring robustness and generalization in extreme degradation scenarios. **In phase II**, we train RLDM in reflectance and illumination domains to estimate Retinex priors from the low-quality image, with the constraint of consistency with those extracted by RPE from the ground-truth image. Therefore, the extracted Retinex priors can guide the RGformer in detail enhancement and illumination correction, resulting in visually appealing results with favorable downstream performance.

Our contributions are summarized as follows:

- We propose a novel DM-based framework, Reti-Diff, for the IDIR task. To the best of our knowledge, this is the first practice of the latent diffusion model to tackle the IDIR problem.

- We propose to let RLDM learn Retinex knowledge and generate high-quality reflectance and illumination priors from the low-quality input, which serve as critical guidance in detail enhancement and illumination correction and can be integrated with various methods.
- We propose RGformer, which integrates extracted Retinex priors to decompose features into reflectance and illumination components. Subsequently, RG-MCA and DFA are employed to refine and aggregate these decomposed features, ensuring robustness and generalization in complex illumination degradation scenarios.
- Extensive experiments on four IDIR tasks verify our superiority, efficiency, and generalizability to existing methods in terms of image quality and favorability in downstream applications, including low-light object detection and image segmentation.

2 Related work

Illumination Degradation Image Restoration. Early IDIR methods mainly include three approaches: histogram equalization (HE) (Cheng & Shi, 2004), gamma correction (GC) (Huang et al., 2012), and Retinex theory (Land, 1977). However, these methods still rely on hand-crafted priors, limiting their generalization ability. With the development of deep learning, methods based on CNNs and transformers (Cai et al., 2023; He et al., 2023a) have succeeded in IDIR. UNIE (Jin et al., 2022) proposed a light-effect suppression network that leverages estimated light-effect layers to mitigate excessive illumination. To improve visibility, NTD (Jin et al., 2023) introduced a nighttime dehazing algorithm to suppress glow while enhancing low-light regions. Besides, Xue *et al.* (Xue et al., 2024) introduced multi-modal visual-language information by integrating wavelet and Fourier transforms with the CLIP-based model prior. To enhance generative capacity, Diff-Retinex (Yi et al., 2023) and GSAD (Jinhui et al., 2023) introduced DM to the IDIR field by directly applying it to image-level generation. However, they entail significant computational costs and may lead to pixel misalignment with the original input, particularly concerning restored image details and local consistency.

Diffusion Models. Diffusion models (DMs) have verified great success in density estimation (Kingma et al., 2021) and data generation (He et al., 2024a). Such a probabilistic generative model adopts a parameterized Markov chain to optimize the lower variational bound on the likelihood function, enabling them to generate target distributions with greater accuracy. Recently, DMs have been introduced to solve the IDIR problem (Yi et al., 2023; Jinhui et al., 2023). However, when directly applied to image-level generation, these methods bring computational burdens and pixel misalignment. To overcome this, we employ LDM to estimate priors within a low-dimensional latent space and then integrate these priors into the transformer-based framework, addressing the above problems. Besides, unlike existing LDM-based methods (Xia et al., 2023; Chen et al., 2023) that solely rely on priors extracted from the RGB domain, our method, tailored to the IDIR task, empowers LDMs to extract Retinex information from both the reflectance and illumination domains. This adaptation allows our method to generate high-fidelity compact Retinex priors directly from low-quality input images but avoid the impact of degradation. By doing so, this novel approach enables us to simultaneously enhance image details using the reflectance prior and correct color distortions with the illumination prior, resulting in visually appealing results with favorable downstream tasks.

3 Methodology

In this paper, we propose Reti-Diff, the pioneering method based on Latent Diffusion Models (LDM) for IDIR tasks. Reti-Diff is specifically tailored to address the challenges inherent in IDIR tasks by leveraging high-quality Retinex priors extracted from both the illumination and reflectance domains to guide the restoration process. This innovative approach utilizes the extracted Retinex prior representation as dynamic modulation parameters, facilitating simultaneous enhancement of restoration details through the reflectance prior and correction of color distortion via the illumination prior. This ensures the generation of visually compelling results while positively impacting downstream tasks.

As shown in Fig. 3, our Reti-Diff comprises two parts: the Retinex-guided transformer (RGformer) and the Retinex-based latent diffusion model (RLDM). To ensure the generation of high-quality priors, Reti-Diff undergoes a two-phase training strategy, involving the initial pretraining of Reti-Diff and the subsequent optimization of RLDM. In this section, we provide an in-depth explanation of the two-phase training approach and elucidate the entire restoration process.

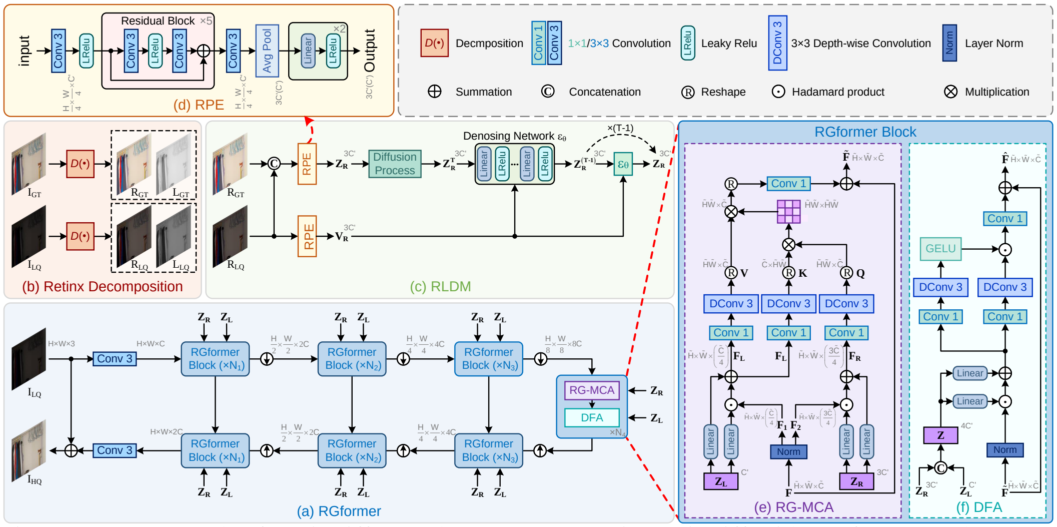

Figure 3: Framework of Reti-Diff. In Phase I, we pretrain Reti-Diff with RGformer and RPE to ensure the robust learning of RLDM and then optimize RLDM to generate high-quality Retinex priors in Phase II, which guide RGformer in detail enhancement and illumination correction. In (a), we omit the auxiliary decoder $D_a(\cdot)$ for simplicity. In panel (c), we illustrate the use of RLDM to extract the reflectance prior; the illumination prior can be extracted similarly. Zoom in for clarity.

3.1 PRETRAIN RETI-DIFF

We first pretrain Reti-Diff to encode the ground truth image into compact priors with Retinex prior extraction (RPE) module and use the extracted Retinex priors to guide RGformer for restoration.

Retinex prior extraction module. Given the low-quality (LQ) image $\mathbf{I}_{LQ} \in \mathbb{R}^{H\times W\times 3}$ and its corresponding ground truth $\mathbf{I}_{GT} \in \mathbb{R}^{H\times W\times 3}$, we initially decompose them into the reflectance image $\mathbf{R} \in \mathbb{R}^{H\times W\times 3}$ and the illumination map $\mathbf{L} \in \mathbb{R}^{H\times W}$ according to Retinex theory:

$$\mathbf{I}_{LQ} = \mathbf{R}_{LQ} \odot \mathbf{L}_{LQ}, \mathbf{I}_{GT} = \mathbf{R}_{GT} \odot \mathbf{L}_{GT}, \tag{1}$$

where $\odot$ is Hadamard product. Following URetinex (Wu et al., 2022), we use a pretrained decomposing network $D(\cdot)$ to decompose $\mathbf{I}_{LQ}$ and $\mathbf{I}_{GT}$, comprising three Conv+LeakyReLU layers and a Conv+ReLU layer. Then we concatenate the corresponding components of ground truth and LQ image and use the RPE module RPE$(\cdot)$ to encode them into Retinex priors $\mathbf{Z_R} \in \mathbb{R}^{3C'}$, $\mathbf{Z_L} \in \mathbb{R}^{C'}$:

$$\mathbf{Z_R} = \text{RPE}(\text{down}(\text{conca}(\mathbf{R}_{GT}, \mathbf{R}_{LQ}))), \quad \mathbf{Z_L} = \text{RPE}(\text{down}(\text{conca}(\mathbf{L}_{GT}, \mathbf{L}_{LQ}))), \tag{2}$$

where conca$(\cdot)$ denotes concatenation and down$(\cdot)$ represents downsampling that is operated by PixelUnshuffle. The Retinex priors, $\mathbf{Z_R}$ and $\mathbf{Z_L}$, are then fed into RGformer to serve as dynamic modulation parameters for detail restoration and color correction.

Retinex-guided transformer. RGformer mainly consists of two parts in each block, *i.e.*, Retinex-guided multi-head cross attention (RG-MCA) and dynamic feature aggregation (DFA) module. In RG-MCA, we first split the input feature $\mathbf{F} \in \mathbb{R}^{\tilde{H}\times\tilde{W}\times\tilde{C}}$ into two parts $\mathbf{F}_1 \in \mathbb{R}^{\tilde{H}\times\tilde{W}\times(3\tilde{C}/4)}$ and $\mathbf{F}_2 \in \mathbb{R}^{\tilde{H}\times\tilde{W}\times(\tilde{C}/4)}$ along the channel dimension. Afterwards, we integrated $\mathbf{Z_R}$ and $\mathbf{Z_L}$ as the corresponding dynamic modulation parameters to generate reflectance-guided feature $\mathbf{F_R} \in \mathbb{R}^{\tilde{H}\times\tilde{W}\times(3\tilde{C}/4)}$ and illumination-guided feature $\mathbf{F_L} \in \mathbb{R}^{\tilde{H}\times\tilde{W}\times(\tilde{C}/4)}$:

$$\mathbf{F_R} = \text{Li}_1(\mathbf{Z_R}) \odot \text{Norm}(\mathbf{F}_1) + \text{Li}_2(\mathbf{Z_R}), \quad \mathbf{F_L} = \text{Li}_1(\mathbf{Z_L}) \odot \text{Norm}(\mathbf{F}_2) + \text{Li}_2(\mathbf{Z_L}), \tag{3}$$

where Norm$(\cdot)$ is layer normalization. Li$(\cdot)$ means linear layer. Afterward, we aggregate global spatial information by projecting $\mathbf{F_R}$ into query $\mathbf{Q} = \mathbf{W}_Q\mathbf{F_R}$ and key $\mathbf{K} = \mathbf{W}_K\mathbf{F_L}$ and transforming $\mathbf{F_L}$ into value $\mathbf{V} = \mathbf{W}_V\mathbf{F_L}$, where $\mathbf{W}$ is the combination of a 1×1 point-wise convolution and a 3×3 depth-wise convolution. We then perform cross-attention and get the output feature $\tilde{\mathbf{F}}$:

$$\tilde{\mathbf{F}} = \mathbf{F} + \text{SoftMax}\left(\mathbf{Q}\mathbf{K}^T/\sqrt{\tilde{C}}\right) \cdot \mathbf{V}. \tag{4}$$

By doing so, RG-MCA introduces explicit guidance to fully exploit Retinex knowledge at the feature level and use cross attention mechanism to implicitly model the Retinex theory and refine the decomposed features, which helps to restore missing details and correct color distortion.

Then we employ DFA for local feature aggregation. Apart from the 1×1 Conv and 3×3 depth-wise Conv for information fusion, DFA adopts GELU, termed $\text{GELU}(\bullet)$, to ensure the flexibility of aggregation (He et al., 2023b). Thus, given $\tilde{\mathbf{F}}$ and $\mathbf{Z}$, where $\mathbf{Z} = \text{conca}(\mathbf{Z}_\mathbf{R}, \mathbf{Z}_\mathbf{L})$, the output $\hat{\mathbf{F}}$ is

$$\hat{\mathbf{F}} = \tilde{\mathbf{F}} + \text{GELU}(\mathbf{W}_1\mathbf{F}') \odot \mathbf{W}_2\mathbf{F}', \;\; \mathbf{F}' = \text{Li}_1(\mathbf{Z}) \odot \text{Norm}(\tilde{\mathbf{F}}) + \text{Li}_2(\mathbf{Z}). \tag{5}$$

Optimization. Having gotten the enhanced result $\mathbf{I}_{HQ}$, we propose a reconstruction loss with L_1 norm $\|\bullet\|_1$ to jointly train RPE and RGformer, which can facilitate the extraction of Retinex priors:

$$L_{Rec} = \|\mathbf{I}_{GT} - \mathbf{I}_{HQ}\|_1. \tag{6}$$

To ensure that the separated features within RG-MCA capture reflectance and illumination knowledge, we use an auxiliary decoder $D_a(\bullet)$ with the same structure as that in (Locatello et al., 2020). $D_a(\bullet)$ takes $\tilde{\mathbf{F}}$ as input and outputs the reconstructed reflectance image $\mathbf{R}_{Re}$ and illumination map $\mathbf{L}_{Re}$. For efficiency, we only apply $D_a(\bullet)$ for the first transformer block in encoder to get $\mathbf{R}^I_{Re}$ and $\mathbf{L}^I_{Re}$ and for the last block in decoder to get $\mathbf{R}^L_{Re}$ and $\mathbf{L}^L_{Re}$. $D_a(\bullet)$ is supervised by a Retinex loss:

$$L_R = \|\mathbf{R}_{LQ} - \mathbf{R}^I_{Re}\|_1 + \|\mathbf{L}_{LQ} - \mathbf{L}^I_{Re}\|_1 + \|\mathbf{R}_{GT} - \mathbf{R}^L_{Re}\|_1 + \|\mathbf{L}_{GT} - \mathbf{L}^L_{Re}\|_1. \tag{7}$$

By constraining the input and output ports, Eq. (7) ensures the preservation of essential Retinex information throughout the network. This integration not only facilitates the incorporation of Retinex theory into the split features but also enhances the overall restoration capability.

In Phase I, the final loss L_{P1} is formulated with the assistance of a hyperparameter λ_1 ($\lambda_1 = 1$):

$$L_{P1} = L_{Rec} + \lambda_1 L_R. \tag{8}$$

3.2 Retinex-based Latent Diffusion Model

In Phase II, we train the RLDM to predict Retinex priors from the low-quality input, which are expected to be consistent with that extracted by RPE from the ground-truth image. Unlike conventional LDMs trained on the RGB domain, we introduce two RLDMs with a Siamese structure and train them on distinct domains: the reflectance domain and the illumination domain. This approach, grounded in Retinex theory, equips our RLDM to generate a more generative reflectance prior $\hat{\mathbf{Z}}_\mathbf{R}$ to enhance image details, and a more harmonized illumination prior $\hat{\mathbf{Z}}_\mathbf{L}$ for color correction. The compact priors retain high-quality information while effectively mitigating the effects of degradation. Note that RLDM is constructed upon the conditional denoising diffusion probabilistic models, with both a forward diffusion process and a reverse denoising process. To simplify, we provide a detailed derivation for $\hat{\mathbf{Z}}_\mathbf{R}$ herein, while that of $\hat{\mathbf{Z}}_\mathbf{L}$ can be found in the appendix.

Diffusion process. In the diffusion process, we first use the pretrained RPE to extract the reflectance prior $\mathbf{Z}_\mathbf{R}$, which is treated as the starting point of the forward Markov process, *i.e.*, $\mathbf{Z}_\mathbf{R} = \mathbf{Z}^0_\mathbf{R}$. We then gradually add Gaussian noise to $\mathbf{Z}_\mathbf{R}$ by T iterations and each iteration can be defined as:

$$q\left(\mathbf{Z}^t_\mathbf{R} | \mathbf{Z}^{t-1}_\mathbf{R}\right) = \mathcal{N}\left(\mathbf{Z}^t_\mathbf{R}; \sqrt{1-\beta^t}\mathbf{Z}^{t-1}_\mathbf{R}, \beta^t\mathbf{I}\right), \tag{9}$$

where $t = 1, \cdots, T$. $\mathbf{Z}^t_\mathbf{R}$ denotes the noisy prior at time step t, β^t is the predefined factor that controls the noise variance, and $\mathcal{N}$ is the Gaussian distribution. Following (Kingma & Welling, 2013), we define $\alpha^t = 1 - \beta^t$ and $\bar{\alpha}^t = \prod_{i=1}^t \alpha^i$, allowing us to simplify Eq. (9) as follows:

$$q\left(\mathbf{Z}^t_\mathbf{R} | \mathbf{Z}^0_\mathbf{R}\right) = \mathcal{N}\left(\mathbf{Z}^t_\mathbf{R}; \sqrt{\bar{\alpha}^t}\mathbf{Z}^0_\mathbf{R}, (1-\bar{\alpha}^t)\mathbf{I}\right). \tag{10}$$

Reverse process. In the reverse process, RLDM aims to extract the reflectance prior from pure Gaussian noise. Thus, RLDM samples a Gaussian random noise map $\mathbf{Z}^T_\mathbf{R}$ and then gradually denoise it to run backward from $\mathbf{Z}^T_\mathbf{R}$ to $\mathbf{Z}^0_\mathbf{R}$ with the corresponding mean μ^t and variance σ^t:

$$p\big(\mathbf{Z}^{t-1}_\mathbf{R} | \mathbf{Z}^t_\mathbf{R}, \mathbf{Z}^0_\mathbf{R}\big) = \mathcal{N}\big(\mathbf{Z}^{t-1}_\mathbf{R}; \boldsymbol{\mu}^t(\mathbf{Z}^t_\mathbf{R}, \mathbf{Z}^0_\mathbf{R}), (\boldsymbol{\sigma}^t)^2\mathbf{I}\big), \tag{11}$$

where $\boldsymbol{\mu}^t(\mathbf{Z}^t_\mathbf{R}, \mathbf{Z}^0_\mathbf{R}) = \frac{1}{\sqrt{\alpha^t}}(\mathbf{Z}^t_\mathbf{R} - \frac{1-\alpha^t}{\sqrt{1-\bar{\alpha}^t}}\boldsymbol{\epsilon})$ and $(\boldsymbol{\sigma}^t)^2 = \frac{1-\bar{\alpha}^{t-1}}{1-\bar{\alpha}^t}\beta^t$. $\boldsymbol{\epsilon}$ is the noise in $\mathbf{Z}^t_\mathbf{R}$ and we employ a denoising network $\boldsymbol{\epsilon}_\theta(\bullet)$ to estimate θ. To operate in the latent space, we further introduce another RPE module $\widetilde{\text{RPE}}(\bullet)$ to extract the conditional reflectance vector $\mathbf{V}_\mathbf{R} \in \mathbb{R}^{3C'}$ from the reflectance image $\mathbf{R}_{LQ}$ of the LQ image, *i.e.*, $\mathbf{V}_\mathbf{R} = \widetilde{\text{RPE}}(\text{down}(\mathbf{R}_{LQ}))$. Therefore, the denoising network can be represented by $\boldsymbol{\epsilon}_\theta\left(\mathbf{Z}^t_\mathbf{R}, \mathbf{V}_\mathbf{R}, t\right)$. By setting the variance to $1 - \alpha^t$, we get

$$\mathbf{Z}^{t-1}_\mathbf{R} = \frac{1}{\sqrt{\alpha^t}}(\mathbf{Z}^t_\mathbf{R} - \frac{1-\alpha^t}{\sqrt{1-\bar{\alpha}^t}}\boldsymbol{\epsilon}_\theta(\mathbf{Z}^t_\mathbf{R}, \mathbf{V}_\mathbf{R}, t)) + \sqrt{1-\alpha^t}\boldsymbol{\epsilon}^t, \tag{12}$$

Methods	Sources	*LOL-v1*				*LOL-v2-real*				*LOL-v2-synthetic*				*SID*			
		PSNR ↑	SSIM ↑	FID ↓	BIQE ↓	PSNR ↑	SSIM ↑	FID ↓	BIQE ↓	PSNR ↑	SSIM ↑	FID ↓	BIQE ↓	PSNR ↑	SSIM ↑	FID ↓	BIQE ↓
MIRNet (Zamir et al., 2020)	ECCV20	24.14	0.835	71.16	47.75	20.02	0.820	82.25	41.18	21.94	0.876	40.18	36.29	20.84	0.605	81.37	40.63
EnGAN (Jiang et al., 2021)	TIP21	17.48	0.656	153.98	35.82	18.23	0.617	173.28	51.06	16.57	0.734	93.66	45.59	17.23	0.543	77.52	33.47
RUAS (Liu et al., 2021)	CVPR21	18.23	0.723	127.60	45.17	18.27	0.723	151.62	34.73	16.55	0.652	91.60	46.38	18.44	0.581	72.18	45.02
IPT (Chen et al., 2021)	CVPR21	16.27	0.504	158.83	29.35	19.80	0.813	97.24	31.17	18.30	0.811	76.79	42.15	20.53	0.618	70.58	36.71
URetinex (Wu et al., 2022)	CVPR22	21.33	0.835	85.59	30.37	20.44	0.806	76.74	28.85	24.73	0.897	33.25	33.46	22.09	0.633	71.58	38.44
UFormer (Wang et al., 2022)	CVPR22	16.36	0.771	166.69	41.06	18.82	0.771	164.41	40.36	19.66	0.871	58.69	39.75	18.54	0.577	100.14	42.13
Restormer (Zamir et al., 2022)	CVPR22	22.43	0.823	78.75	33.18	19.94	0.827	114.35	37.27	21.41	0.830	46.89	35.06	22.27	0.649	75.47	32.49
SNR-Net (Xu et al., 2022)	CVPR22	24.61	0.842	66.47	28.73	21.48	0.849	68.56	28.83	24.14	0.928	30.52	33.47	22.87	0.625	74.78	30.08
SMG (Xu et al., 2023)	CVPR23	24.82	0.838	69.47	30.15	22.62	0.857	71.76	30.32	25.62	0.905	23.36	29.35	23.18	0.644	77.58	31.50
PyDiff (Zhou et al., 2023a)	IJCAI23	21.15	0.857	**49.47**	21.13	—	—	—	—	—	—	—	—	—	—	—	—
Retformer (Cai et al., 2023)	ICCV23	25.16	0.845	72.38	26.68	**22.80**	0.840	79.58	34.39	25.67	0.930	22.78	30.26	24.44	0.680	82.64	35.04
Diff-Retinex (Yi et al., 2023)	ICCV23	21.98	0.852	51.33	**19.62**	20.17	0.826	**46.67**	**24.18**	24.30	0.921	28.74	26.35	23.62	0.665	**58.93**	31.17
MRQ (Liu et al., 2023)	ICCV23	**25.24**	0.855	53.32	22.73	22.37	0.854	68.89	33.61	25.54	0.940	20.86	25.09	24.62	0.683	61.09	**27.81**
IAGC (Wang et al., 2023)	ICCV23	24.53	0.842	59.73	25.50	22.20	**0.863**	70.34	31.70	25.58	0.941	21.38	30.32	**24.80**	**0.688**	63.72	29.53
DiffIR (Xia et al., 2023)	ICCV23	23.15	0.828	70.13	26.38	21.15	0.816	72.33	29.15	24.76	0.921	28.87	27.74	23.17	0.640	78.80	30.56
CUE (Zheng et al., 2023)	ICCV23	21.86	0.841	69.83	27.15	21.19	0.829	67.05	28.83	24.41	0.917	31.33	33.83	23.25	0.652	77.38	28.85
GSAD (Jinhui et al., 2023)	NIPS23	23.23	0.852	51.64	19.96	20.19	0.847	46.77	28.85	24.22	0.927	**19.24**	25.76	—	—	—	—
AST (Zhou et al., 2024)	CVPR24	21.09	0.858	87.67	21.23	21.68	0.856	91.81	25.17	22.25	0.927	37.19	28.78	—	—	—	—
MambaIR (Guo et al., 2024)	ECCV24	22.23	**0.863**	63.39	20.17	21.15	0.857	56.09	24.46	**25.75**	**0.958**	19.75	**20.37**	21.14	0.656	154.76	32.72
Reti-Diff	Ours	**25.35**	**0.866**	**49.14**	**17.75**	**22.97**	**0.858**	**43.18**	**23.66**	**27.53**	**0.951**	**13.26**	**15.77**	**25.53**	**0.692**	**51.66**	**25.58**

Table 1: Results on the LLIE task. The best two results are in **red** and **blue** fonts, respectively.

where $\boldsymbol{\epsilon}^t \sim \mathcal{N}(0, \mathbf{I})$. By using Eq. (12) for T iterations, we can get the predicted prior $\hat{\mathbf{Z}}_{\mathbf{R}}$ and use it to guide RGformer for image restoration. Because the size of the predicted prior $\hat{\mathbf{Z}}_{\mathbf{R}} \in \mathbb{R}^{3C'}$ is much smaller than the original reflectance image $\mathbf{R}_{LQ} \in \mathbb{R}^{H \times W \times C}$, RLDM needs much less iterations than those image-level diffusion models (Yi et al., 2023). Thus, we can run the complete T iterations for the prior generation rather than randomly selecting one time step.

Optimization. We propose the diffusion loss to restrict the predicted priors $\hat{\mathbf{Z}}_{\mathbf{R}}$ and $\hat{\mathbf{Z}}_{\mathbf{L}}$, generated by two RLDMs with specific weights, to be consistent with those extracted from the ground truth:

$$L_{Dif} = \|\mathbf{Z}_{\mathbf{R}} - \hat{\mathbf{Z}}_{\mathbf{R}}\|_1 + \|\mathbf{Z}_{\mathbf{L}} - \hat{\mathbf{Z}}_{\mathbf{L}}\|_1. \tag{13}$$

For restoration quality, we propose joint training RPE, RGformer, and RLDM with the Phase II loss:

$$L_{P2} = L_{Dif} + \lambda_2 L_{Rec} + \lambda_3 L_R, \tag{14}$$

where λ_2 and λ_3 are two hyper-parameters and are set as 1 in this paper. The constraints imposed by L_R and L_{Dif}, combined with our approach to extracting Retinex priors in a compact space, ensure the generation of high-quality priors that significantly reduce interference from degraded inputs.

3.3 Inference

In the inference phase, given the LQ input $\mathbf{I}_{LQ}$, Reti-Diff first uses $\widetilde{\text{RPE}}$ to extract the conditional vectors $\mathbf{V}_{\mathbf{R}}$ and $\mathbf{V}_{\mathbf{L}}$, and then generates predicted Retinex priors $\hat{\mathbf{Z}}_{\mathbf{R}}$ and $\hat{\mathbf{Z}}_{\mathbf{L}}$ with two RLDMs. Under the guidance of the Retinex priors, RGformer generates the restored HQ image $\mathbf{I}_{HQ}$. Benefiting from our Retinex-based diffusion framework, $\mathbf{I}_{HQ}$ enjoys richer texture details and more harmonized illumination, presenting visual-appealing results and further enhancing downstream tasks.

4 Experiment

4.1 Experimental Setup

Our Reti-Diff is implemented in PyTorch on four RTX4090 GPUs and is optimized by Adam with momentum terms $(0.9, 0.999)$. In phases I and II, we train the network for 300K iterations and the learning rate is initialized as 2×10^{-4} and gradually reduced to 1×10^{-6} with the cosine annealing (Loshchilov, 2016). Random rotation and flips are used for augmentation. Reti-Diff comprises RLDM and RGformer. For RLDM, the channel number C' and the total time step T are set as 64 and 4. $\beta^{1:T}$ linearly increase from $\beta^1 = 0.1$ to $\beta^T = 0.99$. RGformer adopts a 4-level cascade structure. We set the number of transformer blocks, the attention heads, the channel number as $[3, 3, 3, 3]$, $[1, 2, 4, 8]$, $[64, 128, 256, 512]$ from level 1 to 4. We abandon GT-mean for fairness.

4.2 Comparative Evaluation

Low-light Image Enhancement. We conduct experiments on four datasets: *LOL-v1* (Wei et al., 2018), *LOL-v2-real* (Yang et al., 2021), *LOL-v2-syn* (Yang et al., 2021), and *SID* (Chen et al., 2019), and involves four metrics: PSNR, SSIM, FID (Heusel et al., 2017), and BIQE (Moorthy & Bovik, 2010). Larger PSNR and SSIM, as well as smaller FID and BIQE, denote superior results. Adhering to the training manner in (Cai et al., 2023), we compare our method against 17 cutting-edge techniques and report the results in Table 1. As depicted in Table 1, our method emerges as the top performer across all datasets, surpassing the second-best method (Diff-Retinex) by 13.2%, un-

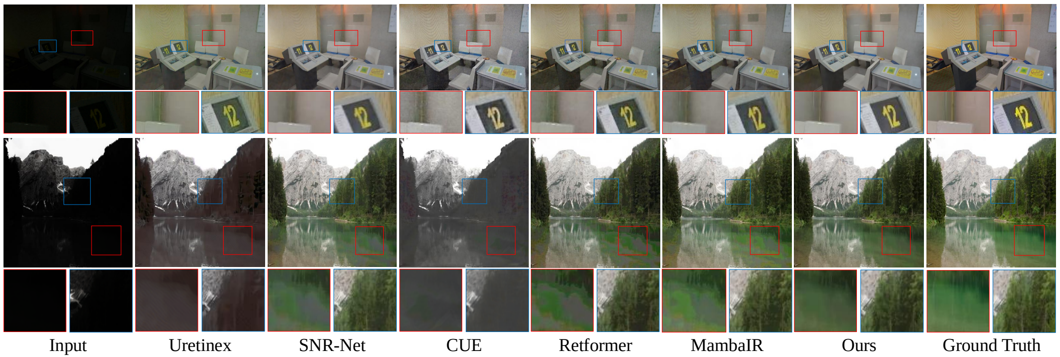

Figure 4: Visual results on the low-light image enhancement (LLIE) task.

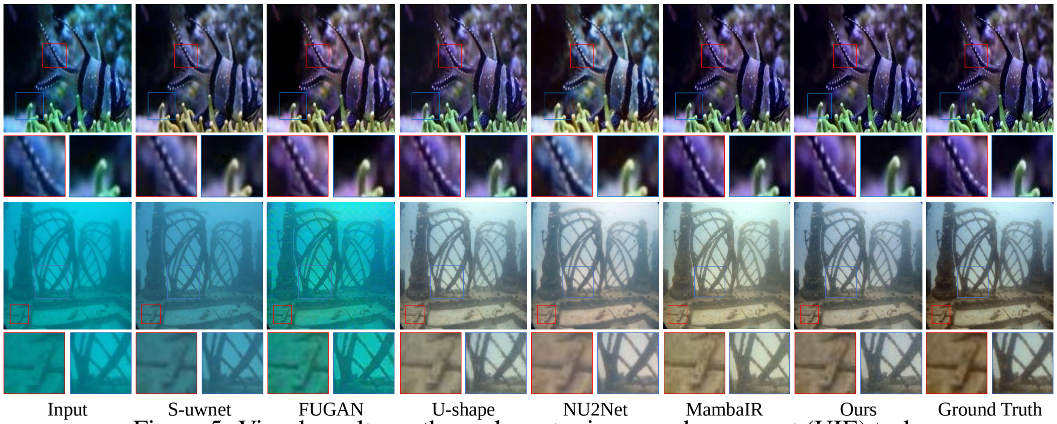

Figure 5: Visual results on the underwater image enhancement (UIE) task.

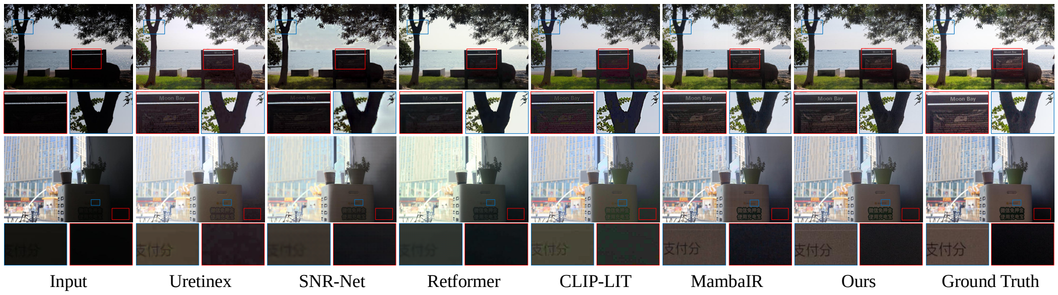

Figure 6: Visual results on the backlit image enhancement (BIE) task.

derscoring our superiority. Fig. 4 presents qualitative results, showcasing our capacity to generate restored images with corrected illumination and enhanced texture, even in extremely challenging conditions. In contrast, existing methods struggle to address these challenges, such as the boundaries of power lines, color distribution of lakes, and textures of wooded areas. Besides, we also compare the efficiency of the diffusion model-based methods with the size of 256×256. As shown in Table 2, our Reti-Diff has the lowest MACs, highest FPS, and the second smallest parameters. This efficiency can be attributed to our utilization of the diffusion model within a low-dimensional compact latent space. For fairness, results from the compared methods are generated by their provided models.

Metrics	Diff-Retinex	PyDiff	GSAD	Ours
Parameter (M)	56.88	97.89	**17.17**	26.11
MACs (G)	396.32	459.69	1340.63	**156.55**
FPS	4.25	3.63	2.33	**12.27**

Table 2: Efficiency analysis in diffusion model-based methods.

Underwater Image Enhancement. We select two widely-used underwater image enhancement datasets: *UIEB* (Li et al., 2019) and *LSUI* (Peng et al., 2023). In addition to PSNR and SSIM, we employ two metrics tailored for underwater images, namely UCIQE (Yang & Sowmya, 2015) and UIQM (Panetta et al., 2015). In all cases, higher values indicate better performance. The results are presented in Table 3. As shown in Table 3, our method achieves the highest performance and outperforms the second-best method (MambaIR) by 2.30%. A qualitative analysis is presented in Fig. 5, illustrating our capacity to correct underwater color aberrations and highlight texture details.

Methods	Sources	*UIEB*				*LSUI*			
		PSNR ↑	SSIM ↑	UCIQE ↑	UIQM ↑	PSNR ↑	SSIM ↑	UCIQE ↑	UIQM ↑
FUGAN (Islam et al., 2020)	IRAL20	17.41	0.842	0.527	2.614	22.16	0.837	0.576	2.667
EnGAN (Jiang et al., 2021)	TIP21	17.73	0.833	0.529	2.465	19.30	0.851	0.587	2.817
Ucolor (Li et al., 2021)	TIP21	20.78	0.868	0.537	3.049	22.91	0.886	0.594	2.735
S-uwnet (Naik et al., 2021)	AAAI21	18.28	0.855	0.544	2.942	20.89	0.875	0.582	2.746
PUIE (Fu et al., 2022)	ECCV22	21.38	0.882	0.566	**3.021**	23.70	0.902	0.605	2.974
U-shape (Peng et al., 2023)	TIP23	22.91	0.905	0.592	2.896	24.16	**0.917**	0.603	3.022
PUGAN (Cong et al., 2023)	TIP23	**23.05**	0.897	0.608	2.902	25.06	0.916	0.629	3.106
ADP (Zhou et al., 2023b)	IJCV23	22.90	0.892	0.621	3.005	24.28	0.913	0.626	3.075
NU2Net (Guo et al., 2023)	AAAI23	22.38	0.903	0.587	2.936	25.07	0.908	0.615	3.112
AST (Zhou et al., 2024)	CVPR24	22.19	0.908	0.602	2.981	27.46	0.916	**0.632**	3.107
MambaIR (Guo et al., 2024)	ECCV24	22.60	**0.939**	**0.617**	2.991	**27.68**	0.916	0.630	**3.118**
Reti-Diff	Ours	**24.12**	**0.910**	**0.631**	**3.088**	**28.10**	**0.929**	**0.646**	**3.208**

Table 3: Results on the UIE task.

Methods	Sources	*BAID*			
		PSNR ↑	SSIM ↑	LPIPS ↓	FID ↓
EnGAN (Jiang et al., 2021)	TIP21	17.96	0.819	0.182	43.55
RUAS (Liu et al., 2021)	CVPR21	18.92	0.813	0.262	40.07
URetinex (Wu et al., 2022)	CVPR22	19.08	0.845	0.206	42.26
SNR-Net (Xu et al., 2022)	CVPR22	20.86	0.860	0.213	39.73
Restormer (Zamir et al., 2022)	CVPR22	21.07	0.832	0.192	41.17
Retformer (Cai et al., 2023)	ICCV23	22.03	0.862	0.173	45.27
CLIP-LIT (Liang et al., 2023)	ICCV23	21.13	0.853	0.159	37.30
Diff-Retinex (Yi et al., 2023)	ICCV23	22.07	0.861	0.160	38.07
DiffIR (Xia et al., 2023)	ICCV23	21.10	0.835	0.175	40.35
AST (Zhou et al., 2024)	CVPR24	22.61	0.851	0.156	32.47
MambaIR (Guo et al., 2024)	ECCV24	**23.07**	**0.874**	**0.153**	**29.13**
Reti-Diff	Ours	**23.19**	**0.876**	**0.147**	**27.47**

Table 4: Results on the BIE task.

Methods	Sources	*DICM*		*LIME*		*MEF*		*NPE*		*VV*	
		PI ↓	NIQE ↓	PI ↓	NIQE ↓	PI ↓	NIQE ↓	PI ↓	NIQE ↓	PI ↓	NIQE ↓
EnGAN (Jiang et al., 2021)	TIP21	4.173	4.064	3.669	4.593	4.015	4.705	3.226	3.993	3.386	4.047
KinD++ (Zhang et al., 2021b)	IJCV21	3.835	3.898	3.785	4.908	4.016	4.557	3.179	3.915	3.773	3.822
SNR-Net (Xu et al., 2022)	CVPR22	3.585	4.715	3.753	5.937	3.677	6.449	3.278	6.446	3.503	9.506
DCC-Net (Zhang et al., 2022)	CVPR22	3.630	3.709	**3.312**	**4.425**	**3.424**	4.598	**2.878**	**3.706**	3.615	**3.286**
UHDFor (Li et al., 2023)	ICLR23	3.684	4.575	4.124	4.430	3.813	4.231	3.135	3.867	3.319	4.330
PairLIE (Fu et al., 2023)	CVPR23	3.685	4.034	3.387	4.587	4.133	4.065	3.726	4.187	**3.334**	3.574
GDP (Fei et al., 2023)	CVPR23	**3.552**	4.358	4.115	4.891	3.694	4.609	3.097	4.032	3.431	4.683
GSAD (Jinhui et al., 2023)	NIPS23	—	**3.465**	—	4.517	—	**3.815**	—	3.806	—	3.355
Reti-Diff	Ours	**2.351**	**3.255**	**2.837**	**3.693**	**3.308**	**3.792**	**2.599**	**3.384**	**3.341**	**3.000**

Table 5: Results on the real-world IDIR task.

Datasets		*L-v2-r*		*L-v2-s*	
Metrics		PSNR ↑	SSIM ↑	PSNR ↑	SSIM ↑
RLDM	w/o RLDM	21.25	0.822	25.38	0.918
	w/o DM	21.72	0.830	25.83	0.927
RGformer	w/o DFA	22.26	0.840	26.49	0.925
	w/o RG-MCA	21.73	0.840	25.92	0.913
	w/o $D_a(\cdot)$	22.58	0.847	26.80	0.944
Train	w/o joint	22.83	0.853	27.18	0.947
Reti-Diff (Ours)		**22.97**	**0.858**	**27.53**	**0.951**

Table 6: Break down ablation.

Backlit Image Enhancement. Following CLIP-LIT (Liang et al., 2023), we select the *BAID* (Lv et al., 2022) dataset for network training. Apart from PSNR and SSIM, our evaluation also selects two perception metrics: LPIPS (Zhang et al., 2018) and FID (Heusel et al., 2017), where lower values denote better performance. We report our results in Table 4. As demonstrated in Table 4, our method outperforms all other methods across all metrics. Besides, a visual comparison in Fig. 6 provides additional evidence of our superiority in detail reconstruction and color correction.

Real-world Illumination Degradation Image Restoration. We also explore our applicability in real-world IDIR tasks. Following CIDNet (Feng et al., 2024), we selected five commonly-used real-world datasets, *i.e.*, *DICM* (Lee et al., 2013), *LIME* (Guo et al., 2016), *MEF* (Wang et al., 2013), *NPE* (Ma et al., 2015), and *VV* (He et al., 2024b), which only have low-quality images without paired ground truths. Therefore, akin to (Feng et al., 2024), we leverage the model pretrained on *LOL-v2-syn* for inference and select PI (Blau et al., 2018) and NIQE (Mittal et al., 2012) as evaluation metrics, where lower scores indicate better results. As presented in Table 5, our method achieves optimal results and surpasses the second-based method (DCC-Net (Zhang et al., 2022)) by 13.39%. This verifies the generalizability of our Reti-Diff in addressing unknown degradation scenarios.

4.3 Ablation Study

We conduct ablation studies on the low-light image enhancement task with the *L-v2-r* and *L-v2-s* datasets, which are short for *LOL-v2-real* and *LOL-v2-syn*. Here, we present a subset of the significant ablation studies; more experiments can be found in the Supplementary Material (Supp).

Effect of RLDM. As shown in Tables 6 and 7, we ablate RLDM by directly removing RLDM, replacing the diffusion model with a linear model that shares the same structure with the denoising network (w/o DM), or retraining RLDM in the RGB domain, *i.e.*, w/o $\mathbf{Z}$, rather than in the reflectance and illumination domain (RGformer is guided by one RGB prior instead). The three changes bring significant performance drops, underscoring the critical role of RLDM in enhancing the restoration process and the importance of using the diffusion model to extract compact priors.

Effect of RGformer. We analyze the impact of our RGformer by removing key modules, such as DFA, RG-MCA, and the auxiliary decoder $D_a(\cdot)$. As shown in Table 6, the outcomes indicate performance decreases when these modules are removed, highlighting their essential roles. Additionally, we also conduct an evaluation to affirm the significance of joint training in our method.

Effect of Retinex priors. We explore the effect of our Retinex prior from three aspects: **(1)** We conduct the break down ablation for the Retinex priors and report the results in Fig. 7 and Table 7. These findings demonstrate the effect of our Reflectance prior $\mathbf{Z_R}$ in detail enhancement and our Illumination prior $\mathbf{Z_L}$ in illumination correction. **(2)** We then swap our Retinex priors with those extracted from ground truth. As shown in Fig. 7 and Table 7, the results guided by the swapped ground-truth priors exhibit limited performance gains. This indicates our RLDM can already generate high-quality priors, which is attributed to the constraints in Eqs. 7 and 13 and our approach to extracting Retinex priors in a compact space, significantly reducing interference from degraded inputs. **(3)** We further explore the potential of Retinex priors under extreme conditions where the reflectance or illumination priors exhibit high similarity between low-quality and ground-truth images.

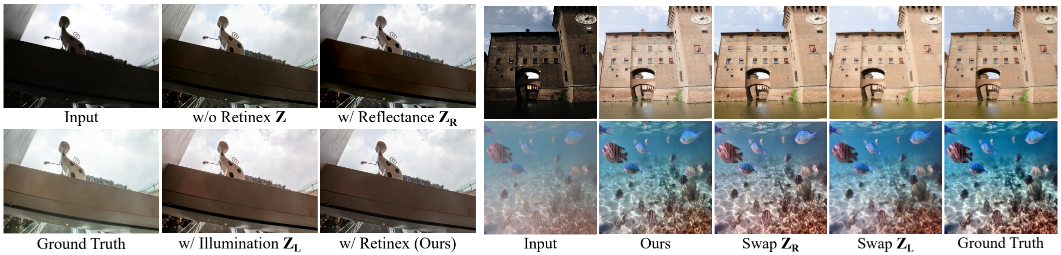

(a) Break down ablation in Retinex priors. (b) Swap our Retinex priors with that extracted from GT.

Figure 7: Visual validation of the effectiveness of Retinex priors.

Dataset	Metrics	All data						Extreme condition (similar in $\mathbf{Z_R}$)				Extreme condition (similar in $\mathbf{Z_L}$)			
		w/o $\mathbf{Z}$	w/ $\mathbf{Z_R}$	w/ $\mathbf{Z_L}$	w/ $\mathbf{Z}$ (Ours)	Swap $\mathbf{Z_R}$	Swap $\mathbf{Z_L}$	w/o $\mathbf{Z}$	w/ $\mathbf{Z_R}$	w/ $\mathbf{Z_L}$	w/ $\mathbf{Z}$ (Ours)	w/o $\mathbf{Z}$	w/ $\mathbf{Z_R}$	w/ $\mathbf{Z_L}$	w/ $\mathbf{Z}$ (Ours)
L-v2-r	PSNR	21.63	22.13	22.35	22.97	23.31	23.17	21.37	21.66	22.57	23.57	21.19	23.06	21.85	24.06
	SSIM	0.830	0.842	0.839	0.858	0.862	0.863	0.823	0.834	0.843	0.862	0.820	0.845	0.831	0.868
L-v2-s	PSNR	26.25	26.62	27.02	27.53	27.92	27.75	25.68	26.17	27.05	28.57	25.42	27.34	26.24	28.80
	SSIM	0.939	0.945	0.941	0.951	0.957	0.956	0.922	0.930	0.951	0.966	0.920	0.958	0.936	0.965

Table 7: Effect of Retinex priors in all data and two extreme conditions (each with 10 images).

Datasets	Metrics	Ufo	Ufo+RLDM	Res	Res+RLDM	Ret	Ret+RLDM
L-v2-r	PSNR	18.82	21.37	19.94	21.56	22.80	23.16
	SSIM	0.771	0.794	0.827	0.837	0.840	0.849
	Gain	–	8.27%	–	4.67%	–	1.33%
L-v2-s	PSNR	19.66	22.08	21.41	24.15	25.67	26.81
	SSIM	0.871	0.889	0.830	0.862	0.930	0.942
	Gain	–	7.19%	–	8.33%	–	2.87%

Table 8: Generalization of Retinex priors. "Ufo", "Res", and "Ret" are Uformer, Restormer, and Retformer.

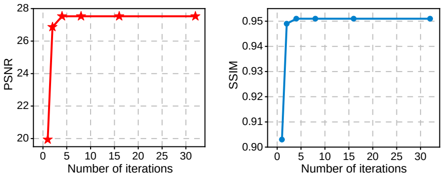

Figure 8: Ablation study of the number of iterations in RLDM on *LOL-v2-syn*.

To validate this, five human subjects rated the similarity of the Retinex priors between low-quality and ground-truth images (the detailed procedure will be introduced in the User Study below). Two sets of images, each with 10 images, were selected based on the highest similarity in reflectance and illumination priors. The results in Table 7 verify the effect of our Retinex priors even in this condition. This is attributed to the generative capacity of our RLDM and the information aggregation capacity of our RGformer. Visual results are placed in the Supp for space limitations.

Generalization of Retinex priors. To assess our generalizability, we incorporate our RLDM into existing cutting-edge methods, namely Ufo (Uformer (Wang et al., 2022)), Res (Restormer (Zamir et al., 2022)) and Ret (Retformer (Cai et al., 2023)), and use the extracted Retinex priors to guide these methods for image enhancement, where the training settings are kept consistent with Reti-Diff. The results are shown in Table 8. Table 8 reveals that RLDM significantly improves the performance of all frameworks, indicating the strong generalization capabilities of our Retinex priors.

Ablations on iteration number. To balance performance and efficiency, we conducted experiments to explore an optimal iteration number T and adjusted β^t in Eq. (9). The results, as shown in Fig. 8, illustrate that Reti-Diff exhibits rapid convergence and generates stable guidance priors in just 4 iterations, which is attributed to the use of the diffusion model within the compact latent space.

4.4 User Study and Downstream Tasks

User Study. We conduct a user study to assess the subjective visual perception of low-light image enhancement. In this study, 29 human subjects are invited to assign scores to the enhanced results based on four criteria: (1) The presence of underexposed or overexposed regions. (2) The existence of color distortion. (3) The occurrence of undesired noise or artifacts. (4) The inclusion of essential structural details. Participants rate the results on a scale from 1 (worst) to 5 (best). Each low-light image is presented alongside its enhanced results, with the names of the enhancement methods concealed. The scores are reported in Table 9, where our method receives the highest scores across all four datasets. This highlights our effectiveness in generating visually appealing results.

Low-light Object Detection. The enhanced images are expected to have better downstream performance. We first verify this on low-light object detection. Following (Cai et al., 2023), all compared methods are performed on *ExDark* (Loh & Chan, 2019) with YOLO, which is retrained from scratch with their own enhanced results. As shown in Table 10, our Reti-Diff exhibits a substantial advantage over existing methods and our performance surpasses that of the second-best method, Retformer, by 4.72%, verifying our efficacy in facilitating high-level vision understanding.

Methods	*L-v1*	*L-v2-r*	*L-v2-s*	*SID*	Mean
KinD	2.31	2.25	2.46	2.33	2.34
EnGAN	2.63	1.69	2.23	1.24	1.95
RUAS	3.57	3.06	3.01	2.23	2.97
Restormer	3.26	3.32	3.41	2.53	3.13
Uretinex	**3.82**	3.98	3.70	3.28	3.70
SNR-Net	3.76	**4.12**	3.58	**3.42**	**3.72**
CUE	3.62	3.81	3.28	3.09	3.45
Retformer	3.35	4.02	**3.71**	3.35	3.61
Ours	**4.05**	**4.33**	**3.92**	**3.75**	**4.01**

Table 9: User study.

Methods (AP)	Bicycle	Boat	Bottle	Bus	Car	Cat	Chair	Cup	Dog	Motor	People	Table	Mean
Baseline	74.7	64.9	70.7	84.2	79.7	47.3	58.6	67.1	64.1	66.2	73.9	45.7	66.4
RetinexNet	72.8	66.4	67.3	87.5	80.6	52.8	60.0	67.8	68.5	**69.3**	71.3	46.2	67.5
KinD	73.2	67.1	64.6	86.8	79.5	58.7	63.4	67.5	67.4	62.3	**75.5**	51.4	68.1
MIRNet	74.9	69.7	68.3	89.7	77.6	57.8	56.9	66.4	69.7	64.6	74.6	53.4	68.6
RUAS	75.7	71.2	73.5	90.7	80.1	59.3	**67.0**	66.3	68.3	66.9	72.6	50.6	70.2
Restormer	77.0	71.0	68.8	**91.6**	77.1	62.5	57.3	**68.0**	69.6	69.2	74.6	49.7	69.7
SCI	73.4	68.0	69.5	86.2	74.5	63.1	59.5	61.0	67.3	63.9	73.2	47.3	67.2
SNR-Net	**78.3**	74.2	**74.5**	89.6	**82.7**	**66.8**	66.3	62.5	74.7	63.1	73.3	**57.2**	71.9
Retformer	78.1	**74.5**	74.2	91.2	82.2	65.0	63.3	67.0	**75.4**	68.6	75.3	55.6	**72.5**
Ours	**82.0**	**77.9**	**76.4**	**92.2**	**83.3**	**69.6**	**67.4**	**74.4**	**75.5**	**74.3**	**78.3**	**57.9**	**75.8**

Table 10: Low-light image detection on *ExDark*.

Methods (IoU)	Bicycle	Boat	Bottle	Bus	Car	Cat	Chair	Dog	Horse	People	Mean
Baseline	43.5	36.3	48.6	70.5	67.3	46.6	11.2	42.4	56.7	57.8	48.1
RetinexNet	48.6	41.7	51.7	77.6	68.3	52.7	15.8	46.3	60.2	62.3	52.5
KinD	51.3	40.2	53.2	76.8	69.4	50.8	14.6	47.3	60.3	60.9	52.5
MIRNet	50.3	42.9	47.4	73.6	62.7	50.4	15.8	46.3	61.0	63.3	51.4
RUAS	53.0	37.3	50.4	71.3	72.3	47.6	15.9	50.8	63.6	60.8	52.3
Restormer	53.8	43.8	51.4	68.7	66.8	52.6	21.6	**54.8**	59.8	63.3	53.7
SCI	54.5	46.3	57.2	78.4	73.3	49.1	22.8	49.0	62.1	66.9	56.0
SNR-Net	**57.7**	**48.6**	**59.5**	**81.3**	**74.8**	50.2	**24.4**	50.7	**64.3**	68.7	**58.0**
Retformer	50.9	47.7	58.6	77.2	68.1	**53.2**	17.4	52.0	61.3	**71.5**	55.8
Ours	**59.8**	**51.5**	**62.1**	**85.5**	**76.6**	**57.7**	**28.9**	**56.3**	**66.2**	**73.4**	**61.8**

Table 11: Low-light semantic segmentation, where images are darkened by (Zhang et al., 2021a).

Methods	*COD10K*				*NC4K*			
	$M\downarrow$	$F_\beta\uparrow$	$E_\phi\uparrow$	$S_\alpha\uparrow$	$M\downarrow$	$F_\beta\uparrow$	$E_\phi\uparrow$	$S_\alpha\uparrow$
Baseline	0.050	0.625	0.812	0.756	0.071	0.733	0.816	0.763
RetinexNet	0.041	0.667	0.845	0.789	0.055	0.750	0.842	0.819
KinD	0.039	0.673	0.849	0.792	0.052	0.762	0.875	0.822
MIRNet	0.037	0.697	0.857	0.799	**0.049**	**0.802**	0.888	0.833
RUAS	**0.036**	0.705	0.861	0.803	0.051	0.795	0.883	0.827
Restormer	**0.036**	0.700	0.859	0.800	0.050	0.792	0.880	0.830
SCI	0.037	**0.710**	0.863	0.805	0.051	0.782	0.880	0.836
SNR-Net	**0.036**	0.703	**0.865**	0.803	**0.049**	0.801	**0.892**	**0.838**
Retformer	0.037	0.682	0.861	**0.806**	0.052	0.766	0.881	0.832
Ours	**0.034**	**0.725**	**0.880**	**0.813**	**0.047**	**0.804**	**0.897**	**0.841**

Table 12: Low-light concealed object segmentation.

Low-light Image Segmentation. We also conducted segmentation tasks and retrained the segmentor for each method following that in detection. **(1)** For semantic segmentation, following (Ju et al., 2022), we apply image darkening to samples from the *VOC* (Everingham et al., 2010) dataset according to (Zhang et al., 2021a). We then employ Mask2Former (Cheng et al., 2022) to segment the enhanced results of these darkened images and select Intersection over Union (IoU) for evaluation. As shown in Table 11, we achieve the highest performance across all classes, surpassing the second-best method by 6.55%. **(2)** We further venture into concealed object segmentation (COS) on two datasets, *COD10K* (Fan et al., 2021) and *NC4K* (Lv et al., 2021), which is a challenging task aimed at delineating objects with inherent background similarity. We also apply image darkening and enlist FEDER (He et al., 2023b) to segment the enhanced results. We evaluate the results using four metrics: mean absolute error (M), adaptive F-measure (F_β), mean E-measure (E_ϕ), and structure measure (S_α). As depicted in Table 12, our method exhibits superior performance compared to the second-best method, SNR-Net, with a margin of 2.16% on average. Note that it is a notable improvement in COS. Collectively, the exceptional results achieved in these two segmentation tasks substantiate our proficiency in recovering image-level illumination degraded information.

5 Discussions

Our Reti-Diff is the first LDM-based solution specifically tailored for the IDIR task, setting it apart from existing LDM-based methods applied in other tasks. To illustrate the distinctions, we compare it with a general enhancement method, DiffIR (Xia et al., 2023): **(1) Motivation.** Reti-Diff targets enhancing details and correcting degraded illumination. Thus, we enable RLDM to learn Retinex knowledge and generate Retinex priors from the low-quality input. We contend that relying solely on priors extracted from the RGB domain struggles to fully represent valuable texture details and correct illumination cues, leading to suboptimal restoration performance. To verify this, we substitute our RLDM for the LDM structure used in DiffIR. In *LOL-v2-syn*, we observe that the PSNR rises from 24.76 to 26.14 and the SSIM increases from 0.921 to 0.933. **(2) Implementation.** Apart from proposing RLDM to extract Retinex priors, we further modify the structure of RGformer to implicitly model the Retinex theory at the feature level and introduce an auxiliary decoder to reconstruct the decomposed Retinex components to the RGB domain. **(3) Performance.** As shown in Table 1, our Reti-Diff significantly outperforms DiffIR (Xia et al., 2023) by 20.6% on average.

6 Conclusions

To balance generation capability and computational efficiency, our approach adopts DM within a compact latent space to generate guidance priors. Specifically, we introduce RLDM to extract Retinex priors, which are subsequently supplied to RGformer for feature decomposition, ensuring precise detailed reconstruction and effective illumination correction. RGformer then refines and aggregates the decomposed features, enhancing the robustness in handling complex degradation scenes. Our approach is validated through extensive experiments, establishing clear superiority.

REFERENCES

Yochai Blau, Roey Mechrez, Radu Timofte, Tomer Michaeli, and Lihi Zelnik-Manor. The 2018 pirm challenge on perceptual image super-resolution. In *ECCV*, pp. 0–0, 2018. 8

Yuanhao Cai, Hao Bian, Jing Lin, Haoqian Wang, Radu Timofte, and Yulun Zhang. Retinexformer: One-stage retinex-based transformer for low-light image enhancement. In *ICCV*, pp. 12504–12513, 2023. 1, 2, 3, 6, 8, 9

Chen Chen, Qifeng Chen, Minh N Do, and Vladlen Koltun. Seeing motion in the dark. In *ICCV*, pp. 3185–3194, 2019. 6

Hanting Chen, Yunhe Wang, Tianyu Guo, Chang Xu, Yiping Deng, Zhenhua Liu, Siwei Ma, Chunjing Xu, Chao Xu, and Wen Gao. Pre-trained image processing transformer. In *CVPR*, pp. 12299–12310, 2021. 6

Zheng Chen, Yulun Zhang, Ding Liu, Bin Xia, Jinjin Gu, Linghe Kong, and Xin Yuan. Hierarchical integration diffusion model for realistic image deblurring. In *NeurIPS*, 2023. 3

Bowen Cheng, Ishan Misra, Alexander G Schwing, Alexander Kirillov, and Rohit Girdhar. Masked-attention mask transformer for universal image segmentation. In *Proceedings of the IEEE/CVF conference on computer vision and pattern recognition*, pp. 1290–1299, 2022. 10

Heng-Da Cheng and XJ Shi. A simple and effective histogram equalization approach to image enhancement. *Digital signal processing*, 14(2):158–170, 2004. 3

Runmin Cong, Wenyu Yang, Wei Zhang, Chongyi Li, Chun-Le Guo, Qingming Huang, and Sam Kwong. Pugan: Physical model-guided underwater image enhancement using gan with dual-discriminators. *IEEE Transactions on Image Processing*, 2023. 8

Mark Everingham, Luc Van Gool, Christopher KI Williams, John Winn, and Andrew Zisserman. The pascal visual object classes (voc) challenge. *International journal of computer vision*, 88: 303–338, 2010. 10

Deng-Ping Fan, Ge-Peng Ji, Ming-Ming Cheng, and Ling Shao. Concealed object detection. *IEEE transactions on pattern analysis and machine intelligence*, 44(10):6024–6042, 2021. 10

Ben Fei, Zhaoyang Lyu, Liang Pan, Junzhe Zhang, Weidong Yang, Tianyue Luo, Bo Zhang, and Bo Dai. Generative diffusion prior for unified image restoration and enhancement. In *CVPR*, pp. 9935–9946, 2023. 8

Yixu Feng, Cheng Zhang, Pei Wang, Peng Wu, Qingsen Yan, and Yanning Zhang. You only need one color space: An efficient network for low-light image enhancement. *arXiv preprint arXiv:2402.05809*, 2024. 8

Xueyang Fu, Delu Zeng, Yue Huang, Yinghao Liao, Xinghao Ding, and John Paisley. A fusion-based enhancing method for weakly illuminated images. *Signal Processing*, 129:82–96, 2016. 1

Zhenqi Fu, Wu Wang, Yue Huang, Xinghao Ding, and Kai-Kuang Ma. Uncertainty inspired underwater image enhancement. In *ECCV*, pp. 465–482. Springer, 2022. 8

Zhenqi Fu, Yan Yang, Xiaotong Tu, Yue Huang, Xinghao Ding, and Kai-Kuang Ma. Learning a simple low-light image enhancer from paired low-light instances. In *CVPR*, pp. 22252–22261, 2023. 8

Chunle Guo, Ruiqi Wu, Xin Jin, Linghao Han, Weidong Zhang, Zhi Chai, and Chongyi Li. Underwater ranker: Learn which is better and how to be better. In *AAAI*, volume 37, pp. 702–709, 2023. 1, 8

Hang Guo, Jinmin Li, Tao Dai, Zhihao Ouyang, Xudong Ren, and Shu-Tao Xia. Mambair: A simple baseline for image restoration with state-space model. In *ECCV*, 2024. 6, 8

Xiaojie Guo, Yu Li, and Haibin Ling. Lime: Low-light image enhancement via illumination map estimation. *IEEE Trans. Image Process.*, 26(2):982–993, 2016. 8

Chunming He, Kai Li, Guoxia Xu, Jiangpeng Yan, Longxiang Tang, Yulun Zhang, Yaowei Wang, and Xiu Li. Hqg-net: Unpaired medical image enhancement with high-quality guidance. *IEEE Transactions on Neural Networks and Learning Systems*, 2023a. 2, 3

Chunming He, Kai Li, Yachao Zhang, Longxiang Tang, Yulun Zhang, Zhenhua Guo, and Xiu Li. Camouflaged object detection with feature decomposition and edge reconstruction. In *CVPR*, pp. 22046–22055, 2023b. 5, 10

Chunming He, Kai Li, Yachao Zhang, Yulun Zhang, Zhenhua Guo, Xiu Li, Martin Danelljan, and Fisher Yu. Strategic preys make acute predators: Enhancing camouflaged object detectors by generating camouflaged objects. 2024a. 3

Chunming He, Yuqi Shen, Chengyu Fang, Fengyang Xiao, Longxiang Tang, Yulun Zhang, Wangmeng Zuo, Zhenhua Guo, and Xiu Li. Diffusion models in low-level vision: A survey. *arXiv preprint arXiv:2406.11138*, 2024b. 8

Martin Heusel, Hubert Ramsauer, Thomas Unterthiner, Bernhard Nessler, and Sepp Hochreiter. Gans trained by a two time-scale update rule converge to a local nash equilibrium. *NeurIPS*, 30, 2017. 6, 8

Shih-Chia Huang, Fan-Chieh Cheng, and Yi-Sheng Chiu. Efficient contrast enhancement using adaptive gamma correction with weighting distribution. *IEEE transactions on image processing*, 22(3):1032–1041, 2012. 3

Md Jahidul Islam, Youya Xia, and Junaed Sattar. Fast underwater image enhancement for improved visual perception. *IEEE Robotics and Automation Letters*, 5(2):3227–3234, 2020. 8

Yifan Jiang, Xinyu Gong, Ding Liu, Yu Cheng, Chen Fang, Xiaohui Shen, Jianchao Yang, Pan Zhou, and Zhangyang Wang. Enlightengan: Deep light enhancement without paired supervision. *IEEE transactions on image processing*, 30:2340–2349, 2021. 2, 6, 8

Yeying Jin, Wenhan Yang, and Robby T Tan. Unsupervised night image enhancement: When layer decomposition meets light-effects suppression. In *ECCV*, pp. 404–421, 2022. 3

Yeying Jin, Beibei Lin, Wending Yan, Yuan Yuan, Wei Ye, and Robby T Tan. Enhancing visibility in nighttime haze images using guided apsf and gradient adaptive convolution. In *ACM MM*, pp. 2446–2457, 2023. 3

HOU Jinhui, Zhiyu Zhu, Junhui Hou, LIU Hui, Huanqiang Zeng, and Hui Yuan. Global structure-aware diffusion process for low-light image enhancement. In *NeurIPS*, 2023. 2, 3, 6, 8

Mingye Ju, Charles A Guo, Chuheng Chen, Jinshan Pan, Jinhui Tang, and Dacheng Tao. Sllen: Semantic-aware low-light image enhancement network. *arXiv preprint arXiv:2211.11571*, 2022. 10

Diederik Kingma, Tim Salimans, Ben Poole, and Jonathan Ho. Variational diffusion models. *NeurIPS*, 34:21696–21707, 2021. 3

Diederik P Kingma and Max Welling. Auto-encoding variational bayes. *arXiv preprint arXiv:1312.6114*, 2013. 5

Edwin H Land. The retinex theory of color vision. *Scientific american*, 237(6):108–129, 1977. 3

Chulwoo Lee, Chul Lee, and Chang-Su Kim. Contrast enhancement based on layered difference representation of 2d histograms. *IEEE Trans. Image Process.*, 22(12):5372–5384, 2013. 8

Chongyi Li, Chunle Guo, Wenqi Ren, Runmin Cong, Junhui Hou, Sam Kwong, and Dacheng Tao. An underwater image enhancement benchmark dataset and beyond. *IEEE Transactions on Image Processing*, 29:4376–4389, 2019. 7

Chongyi Li, Saeed Anwar, Junhui Hou, Runmin Cong, Chunle Guo, and Wenqi Ren. Underwater image enhancement via medium transmission-guided multi-color space embedding. *IEEE Transactions on Image Processing*, 30:4985–5000, 2021. 8

Chongyi Li, Chun-Le Guo, Man Zhou, Zhexin Liang, Shangchen Zhou, Ruicheng Feng, and Chen Change Loy. Embeddingfourier for ultra-high-definition low-light image enhancement. In *ICLR*, 2023. 8

Zhexin Liang, Chongyi Li, Shangchen Zhou, Ruicheng Feng, and Chen Change Loy. Iterative prompt learning for unsupervised backlit image enhancement. In *ICCV*, pp. 8094–8103, 2023. 1, 2, 8

Risheng Liu, Long Ma, Jiaao Zhang, Xin Fan, and Zhongxuan Luo. Retinex-inspired unrolling with cooperative prior architecture search for low-light image enhancement. In *CVPR*, pp. 10561–10570, 2021. 6, 8

Yunlong Liu, Tao Huang, Weisheng Dong, Fangfang Wu, Xin Li, and Guangming Shi. Low-light image enhancement with multi-stage residue quantization and brightness-aware attention. In *ICCV*, pp. 12140–12149, 2023. 6

Francesco Locatello, Dirk Weissenborn, Thomas Unterthiner, Aravindh Mahendran, Georg Heigold, Jakob Uszkoreit, Alexey Dosovitskiy, and Thomas Kipf. Object-centric learning with slot attention. *NeurIPS*, 33:11525–11538, 2020. 5

Yuen Peng Loh and Chee Seng Chan. Getting to know low-light images with the exclusively dark dataset. *Computer Vision and Image Understanding*, 178:30–42, 2019. 9

I Loshchilov. Stochastic gradient descent with warm restarts. In *ICLR*, pp. 1–16, 2016. 6

Xiaoqian Lv, Shengping Zhang, Qinglin Liu, Haozhe Xie, Bineng Zhong, and Huiyu Zhou. Backlitnet: A dataset and network for backlit image enhancement. *Computer Vision and Image Understanding*, 218:103403, 2022. 8

Yunqiu Lv, Jing Zhang, Yuchao Dai, Aixuan Li, Bowen Liu, Nick Barnes, and Deng-Ping Fan. Simultaneously localize, segment and rank the camouflaged objects. In *CVPR*, pp. 11591–11601, 2021. 10

Kede Ma, Kai Zeng, and Zhou Wang. Perceptual quality assessment for multi-exposure image fusion. *IEEE Trans. Image Process.*, 24(11):3345–3356, 2015. 8

Anish Mittal, Rajiv Soundararajan, and Alan C Bovik. Making a "completely blind" image quality analyzer. *IEEE Signal Processing Lett.*, 20(3):209–212, 2012. 8

Anush Krishna Moorthy and Alan Conrad Bovik. A two-step framework for constructing blind image quality indices. *IEEE Signal processing letters*, 17(5):513–516, 2010. 6

Ankita Naik, Apurva Swarnakar, and Kartik Mittal. Shallow-uwnet: Compressed model for underwater image enhancement (student abstract). In *AAAI*, volume 35, pp. 15853–15854, 2021. 8

Karen Panetta, Chen Gao, and Sos Agaian. Human-visual-system-inspired underwater image quality measures. *IEEE Journal of Oceanic Engineering*, 41(3):541–551, 2015. 7

Lintao Peng, Chunli Zhu, and Liheng Bian. U-shape transformer for underwater image enhancement. *IEEE Transactions on Image Processing*, 2023. 7, 8

Neng-Tsann Ueng and Louis L Scharf. The gamma transform: A local time-frequency analysis method. In *ACSSC*, volume 2, pp. 920–924. IEEE, 1995. 1

Shuhang Wang, Jin Zheng, Hai-Miao Hu, and Bo Li. Naturalness preserved enhancement algorithm for non-uniform illumination images. *IEEE Trans. Image Process.*, 22(9):3538–3548, 2013. 8

Yinglong Wang, Zhen Liu, Jianzhuang Liu, Songcen Xu, and Shuaicheng Liu. Low-light image enhancement with illumination-aware gamma correction and complete image modelling network. In *ICCV*, pp. 13128–13137, 2023. 6

Zhendong Wang, Xiaodong Cun, Jianmin Bao, Wengang Zhou, Jianzhuang Liu, and Houqiang Li. Uformer: A general u-shaped transformer for image restoration. In *CVPR*, pp. 17683–17693, 2022. 6, 9

Chen Wei, Wenjing Wang, Wenhan Yang, and Jiaying Liu. Deep retinex decomposition for low-light enhancement. *arXiv preprint arXiv:1808.04560*, 2018. 6

Wenhui Wu, Jian Weng, Pingping Zhang, Xu Wang, Wenhan Yang, and Jianmin Jiang. Uretinex-net: Retinex-based deep unfolding network for low-light image enhancement. In *CVPR*, pp. 5901–5910, 2022. 4, 6, 8

Bin Xia, Yulun Zhang, Shiyin Wang, Yitong Wang, Xinglong Wu, Yapeng Tian, Wenming Yang, and Luc Van Gool. Diffir: Efficient diffusion model for image restoration. In *ICCV*, 2023. 3, 6, 8, 10

Xiaogang Xu, Ruixing Wang, Chi-Wing Fu, and Jiaya Jia. Snr-aware low-light image enhancement. In *CVPR*, pp. 17714–17724, 2022. 6, 8

Xiaogang Xu, Ruixing Wang, and Jiangbo Lu. Low-light image enhancement via structure modeling and guidance. In *CVPR*, pp. 9893–9903, 2023. 6

Minglong Xue, Jinhong He, and Yanyi He. Low-light image enhancement via clip-fourier guided wavelet diffusion. *arXiv:2401.03788*, 2024. 3

Miao Yang and Arcot Sowmya. An underwater color image quality evaluation metric. *IEEE Transactions on Image Processing*, 24(12):6062–6071, 2015. 7

Wenhan Yang, Wenjing Wang, Haofeng Huang, Shiqi Wang, and Jiaying Liu. Sparse gradient regularized deep retinex network for robust low-light image enhancement. *IEEE Transactions on Image Processing*, 30:2072–2086, 2021. 6

Xunpeng Yi, Han Xu, Hao Zhang, Linfeng Tang, and Jiayi Ma. Diff-retinex: Rethinking low-light image enhancement with a generative diffusion model. In *ICCV*, pp. 12302–12311, 2023. 2, 3, 6, 8

Syed Waqas Zamir, Aditya Arora, Salman Khan, Munawar Hayat, Fahad Shahbaz Khan, Ming-Hsuan Yang, and Ling Shao. Learning enriched features for real image restoration and enhancement. In *ECCV*, pp. 492–511. Springer, 2020. 6

Syed Waqas Zamir, Aditya Arora, Salman Khan, Munawar Hayat, Fahad Shahbaz Khan, and Ming-Hsuan Yang. Restormer: Efficient transformer for high-resolution image restoration. In *CVPR*, pp. 5728–5739, 2022. 6, 8, 9

Fan Zhang, Yu Li, Shaodi You, and Ying Fu. Learning temporal consistency for low light video enhancement from single images. In *CVPR*, pp. 4967–4976, 2021a. 10

Richard Zhang, Phillip Isola, Alexei A Efros, Eli Shechtman, and Oliver Wang. The unreasonable effectiveness of deep features as a perceptual metric. In *CVPR*, pp. 586–595, 2018. 8

Yonghua Zhang, Xiaojie Guo, Jiayi Ma, Wei Liu, and Jiawan Zhang. Beyond brightening low-light images. *Int. J. Comput. Vision*, 129:1013–1037, 2021b. 8

Zhao Zhang, Huan Zheng, Richang Hong, Mingliang Xu, Shuicheng Yan, and Meng Wang. Deep color consistent network for low-light image enhancement. In *CVPR*, pp. 1899–1908, 2022. 8

Naishan Zheng, Man Zhou, Yanmeng Dong, Xiangyu Rui, Jie Huang, Chongyi Li, and Feng Zhao. Empowering low-light image enhancer through customized learnable priors. In *ICCV*, pp. 12559–12569, 2023. 6

Dewei Zhou, Zongxin Yang, and Yi Yang. Pyramid diffusion models for low-light image enhancement. *arXiv preprint arXiv:2305.10028*, 2023a. 6

Jingchun Zhou, Qian Liu, Qiuping Jiang, Wenqi Ren, Kin-Man Lam, and Weishi Zhang. Underwater camera: Improving visual perception via adaptive dark pixel prior and color correction. *International Journal of Computer Vision*, pp. 1–19, 2023b. 8

Shihao Zhou, Duosheng Chen, Jinshan Pan, Jinglei Shi, and Jufeng Yang. Adapt or perish: Adaptive sparse transformer with attentive feature refinement for image restoration. In *Proceedings of the IEEE/CVF Conference on Computer Vision and Pattern Recognition (CVPR)*, pp. 2952–2963, June 2024. 6, 8

SUPPLEMENTARY MATERIALS FOR RETI-DIFF: ILLUMINATION DEGRADATION IMAGE RESTORATION WITH RETINEX-BASED LATENT DIFFUSION MODEL

Anonymous authors
Paper under double-blind review

CONTENTS

A METHODOLOGY

A.1 RETINEX-BASED LATENT DIFFUSION MODEL

In this section, we provide a detailed derivation for $\hat{\mathbf{Z}}_{\mathbf{L}}$.

Diffusion process. In the diffusion process, we first use the pretrained RPE to extract the reflectance prior $\mathbf{Z}_{\mathbf{L}}$, which is treated as the starting point of the forward Markov process, *i.e.*, $\mathbf{Z}_{\mathbf{L}} = \mathbf{Z}_{\mathbf{L}}^0$. We then gradually add Gaussian noise to $\mathbf{Z}_{\mathbf{L}}$ by T iterations and each iteration can be defined as:

$$q\left(\mathbf{Z}_{\mathbf{L}}^t|\mathbf{Z}_{\mathbf{L}}^{t-1}\right) = \mathcal{N}\left(\mathbf{Z}_{\mathbf{L}}^t; \sqrt{1-\beta^t}\mathbf{Z}_{\mathbf{L}}^{t-1}, \beta^t\mathbf{I}\right), \tag{1}$$

where $t = 1, \cdots, T$. $\mathbf{Z}_{\mathbf{L}}^t$ denotes the noisy prior at time step t, β^t is the predefined factor that controls the noise variance, and $\mathcal{N}$ is the Gaussian distribution. Following (Kingma & Welling, 2013), Eq. (1) can be simplified as follows:

$$q\left(\mathbf{Z}_{\mathbf{L}}^t|\mathbf{Z}_{\mathbf{L}}^0\right) = \mathcal{N}\left(\mathbf{Z}_{\mathbf{L}}^t; \sqrt{\bar{\alpha}^t}\mathbf{Z}_{\mathbf{L}}^0, (1-\bar{\alpha}^t)\mathbf{I}\right), \tag{2}$$

where $\alpha^t = 1 - \beta^t$ and $\bar{\alpha}^t = \prod_{i=1}^t \alpha^i$.

Reverse process. In the reverse process, RLDM aims to extract the reflectance prior from pure Gaussian noise. Thus, RLDM samples a Gaussian random noise map $\mathbf{Z}_{\mathbf{L}}^T$ and then gradually denoise it to run backward from $\mathbf{Z}_{\mathbf{L}}^T$ to $\mathbf{Z}_{\mathbf{L}}^0$:

$$p\big(\mathbf{Z}_{\mathbf{L}}^{t-1}|\mathbf{Z}_{\mathbf{L}}^t, \mathbf{Z}_{\mathbf{L}}^0\big) = \mathcal{N}\big(\mathbf{Z}_{\mathbf{L}}^{t-1}; \boldsymbol{\mu}^t(\mathbf{Z}_{\mathbf{L}}^t, \mathbf{Z}_{\mathbf{L}}^0), (\boldsymbol{\sigma}^t)^2\mathbf{I}\big), \tag{3}$$

where mean $\boldsymbol{\mu}^t(\mathbf{Z}_{\mathbf{L}}^t, \mathbf{Z}_{\mathbf{L}}^0) = \frac{1}{\sqrt{\alpha^t}}(\mathbf{Z}_{\mathbf{L}}^t - \frac{1-\alpha^t}{\sqrt{1-\bar{\alpha}^t}}\boldsymbol{\epsilon})$ and variance $(\boldsymbol{\sigma}^t)^2 = \frac{1-\bar{\alpha}^{t-1}}{1-\bar{\alpha}^t}\beta^t$. $\boldsymbol{\epsilon}$ denotes the noise in $\mathbf{Z}_{\mathbf{L}}^t$ and is the only uncertain variable. Following previous practice (Xia et al., 2023), we employ a denoising network $\boldsymbol{\epsilon}_\theta(\cdot)$ to estimate θ. To operate in the latent space, we further introduce another RPE module $\widetilde{\mathrm{RPE}}(\cdot)$ to extract the conditional reflectance vector $\mathbf{V}_{\mathbf{L}} \in \mathbb{R}^{C'}$ from

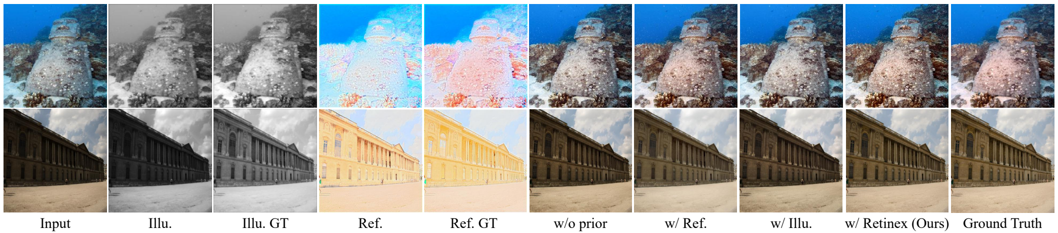

Fig. S1: Effect of Retinex priors in extreme conditions, where the two rows share a similarity in reflectance and illumination components, respectively.

Datasets	Metrics	ℓ_2-norm	ℓ_1-norm (Ours)
L-v2-s	PSNR SSIM	27.26 0.949	27.53 0.951
L-v2-r	PSNR SSIM	22.62 0.853	22.97 0.858

Fig. S1: Effect of ℓ_p-norm in Loss Functions.

Datasets	Metrics	$\lambda_1 = 0.1$	$\lambda_1 = 1$ (Ours)	$\lambda_1 = 10$	$\lambda_2 = 0.1$	$\lambda_2 = 1$ (Ours)	$\lambda_2 = 10$	$\lambda_3 = 0.1$	$\lambda_3 = 1$ (Ours)	$\lambda_3 = 10$
L-v2-s	PSNR SSIM	27.15 0.949	27.53 0.951	27.33 0.948	27.08 0.946	27.53 0.951	27.33 0.947	27.26 0.952	27.53 0.951	27.35 0.946
L-v2-r	PSNR SSIM	22.86 0.857	22.97 0.858	22.82 0.855	22.36 0.851	22.97 0.858	22.76 0.856	22.33 0.853	22.97 0.858	22.16 0.850

Fig. S2: Effect of ℓ_p-norm in Loss Functions.

the reflectance image $\mathbf{L}_{LQ}$ of the LQ image, *i.e.*, $\mathbf{V}_\mathbf{L} = \widetilde{\mathrm{RPE}}(\mathrm{down}(\mathbf{L}_{LQ}))$. Therefore, the denoising network can be represented by $\boldsymbol{\epsilon}_\theta\left(\mathbf{Z}^t_\mathbf{L}, \mathbf{V}_\mathbf{L}, t\right)$. By setting the variance to $1 - \alpha^t$, we get

$$\mathbf{Z}^{t-1}_\mathbf{L} = \frac{1}{\sqrt{\alpha^t}}(\mathbf{Z}^t_\mathbf{L} - \frac{1-\alpha^t}{\sqrt{1-\bar{\alpha}^t}}\boldsymbol{\epsilon}_\theta(\mathbf{Z}^t_\mathbf{L}, \mathbf{V}_\mathbf{L}, t)) + \sqrt{1-\alpha^t}\boldsymbol{\epsilon}^t, \tag{4}$$

where $\boldsymbol{\epsilon}^t \sim \mathcal{N}(0, \mathbf{I})$.

B Experiment

B.1 Ablation Study

Effect of Retinex priors in extreme conditions. We investigate the potential of Retinex priors, *i.e.*, $\mathbf{Z}_\mathbf{R}$ and $\mathbf{Z}_\mathbf{L}$, under extreme conditions where the reflectance or illumination components exhibit high similarity between low-quality and ground-truth images. As shown in Fig. S1, the extracted priors have a diminished effect when the corresponding component shows the similarity between low-quality and ground-truth images. This is because the corresponding component undergoes minimal degradation.

Effect of ℓ_p-norm in Loss Functions. We explore the effect of ℓ_p-norm in loss functions. As shown in Table S1, Reti-Diff achieves better performance when using ℓ_1-norm. Therefore, our loss functions select ℓ_1-norm.

Parameter Analysis. Our Reti-Diff is optimized with multiple losses, which are balanced by three hyperparameters, *i.e.*, λ_1, λ_2, and λ_3. To analyze their impact, we vary one of the parameters and fix others, and report the results in Table S2. Overall, we find that the different coefficients in the tested range only slightly influence the final performance and λ_1, λ_2, and λ_3 obtain better results when they are set to 1. So we set those parameters to 1 each.

B.2 Comparative Evaluation

Low-light Image Enhancement. As shown in Fig. S2, we provide more visualization results. Our method can generate enhanced images with corrected illumination and enhanced texture, even in extremely challenging conditions.

Underwater Image Enhancement. More qualitative analyses are presented in Fig. S3, illustrating our superiority in underwater color correction and fine texture details reconstruction.

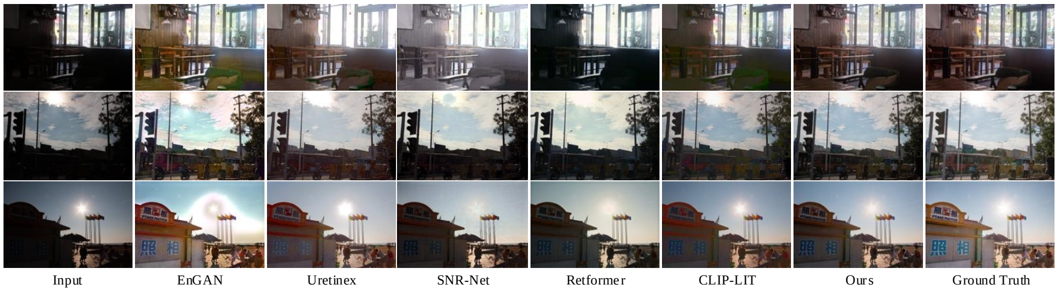

Fig. S2: Visual results on the low-light image enhancement task.

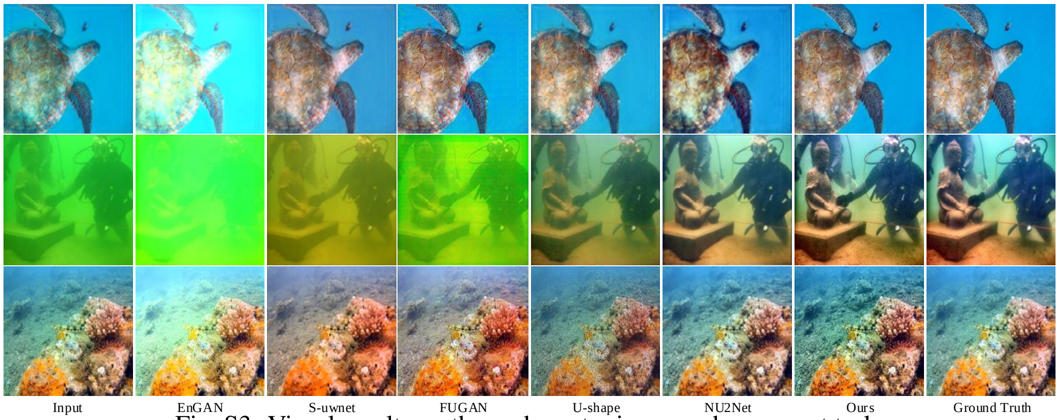

Fig. S3: Visual results on the underwater image enhancement task.

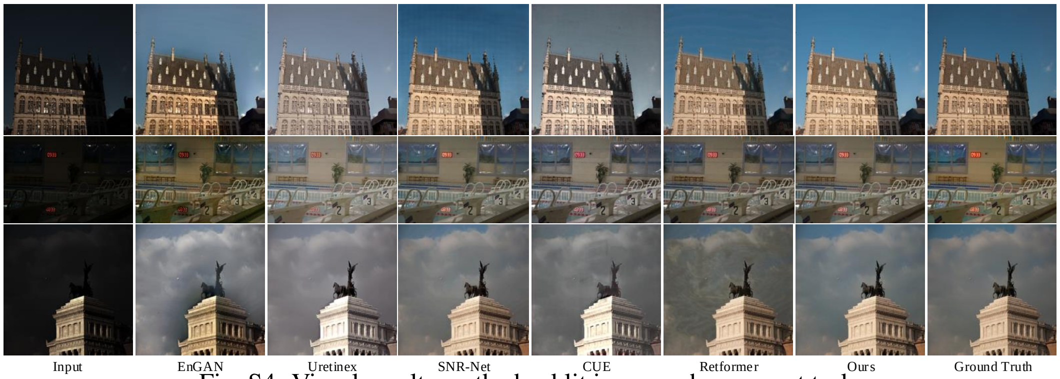

Fig. S4: Visual results on the backlit image enhancement task.

Backlit Image Enhancement. Furthermore, a visual comparison in Fig. S4 provides additional evidence of our superiority in detail reconstruction and color correction. All methods are trained by cropping the training data as 256×256 for fairness.

Real-world Illumination Degradation Image Restoration. As depicted in Fig. S5, our enhanced images demonstrate superior capability in refining texture details and correcting inconsistent illumination, even under real-world complex degradation conditions. It is important to note that ground truth data is not available for these real-world scenarios.

C Downstream Tasks

Low-light Object Detection. As presented in Fig. S7, our method not only enhances image quality but also achieves superior performance in low-light object detection. It is important to note that the ground truth is the same low-quality image as the input.

Low-light Image Segmentation. The low-light image segmentation task comprises two main tasks, *i.e.*, low-light semantic segmentation task and low-light concealed object segmentation task. As depicted in Figs. S8 and S9, our enhanced images result in better segmentation, with masks that capture

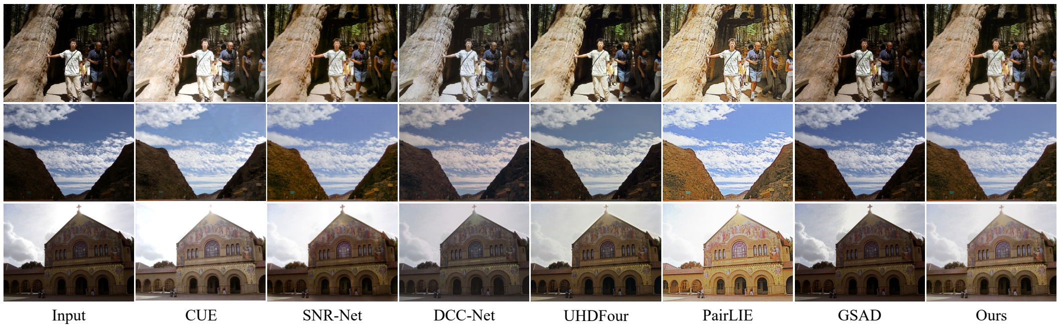

Fig. S5: Visual results on the real-world IDIR task.

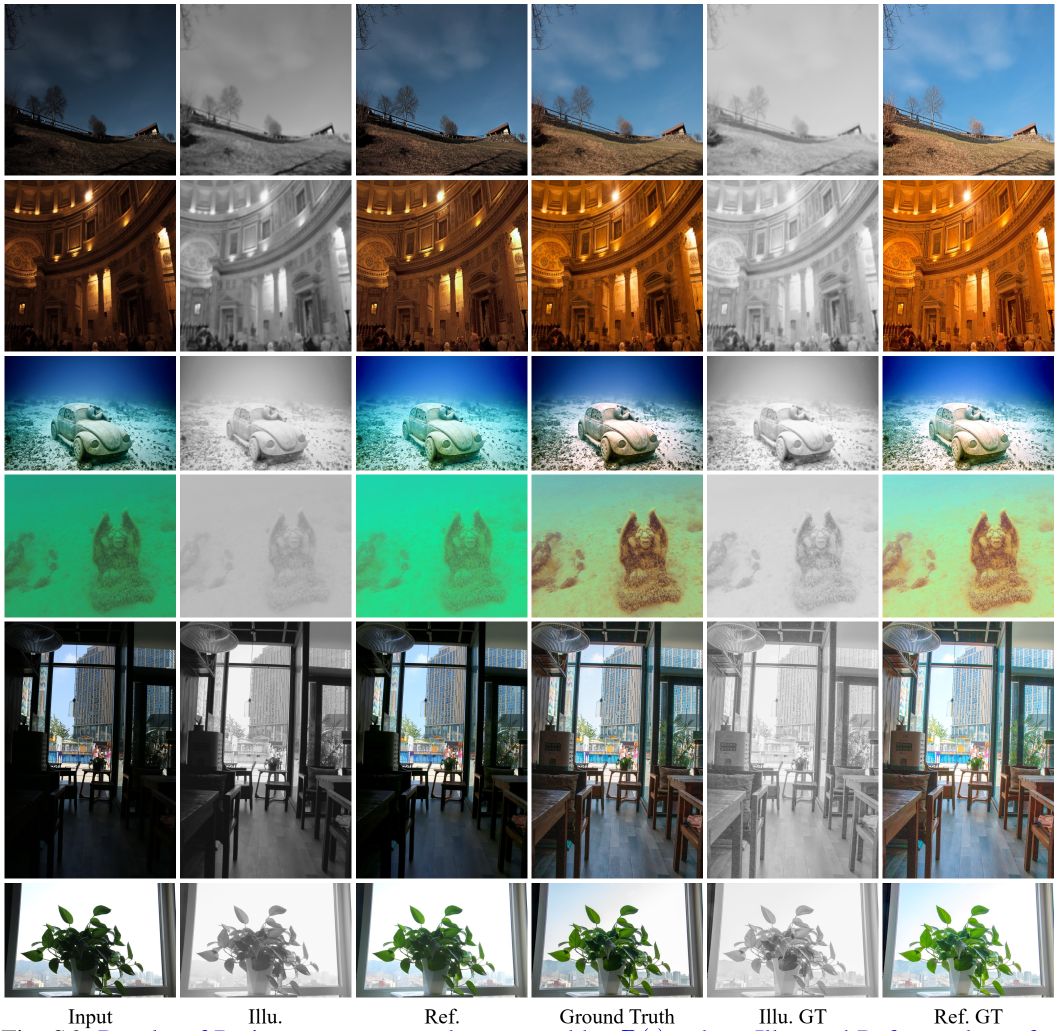

Fig. S6: Results of Retinex components decomposed by $D(\cdot)$, where Illu. and Ref. are shorts for illumination and reflectance.

more complete objects and exhibit more accurate boundaries, further indicating the superiority of our Reti-Diff.

D Limitations and Future Work

In the first image of Fig. S10, our method fails to distinguish the two regions marked by the dashed box due to the ambiguous boundary of the right region and the intrinsic similarities shared between the two areas. Consequently, our method interprets the two distinct regions as a single object and

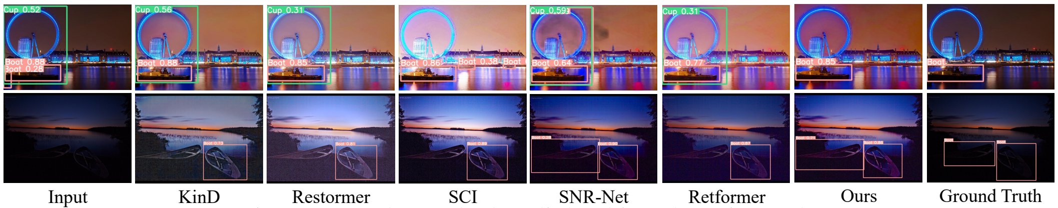

Fig. S7: Results on the low-light object detection task.

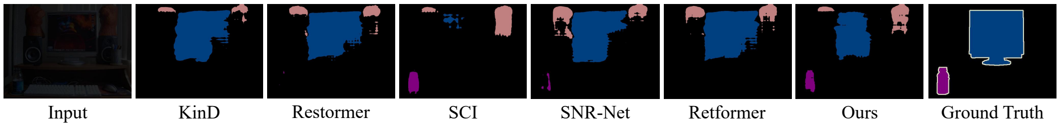

Fig. S8: Results on the low-light semantic segmentation task.

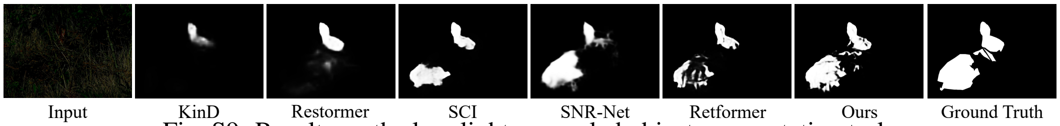

Fig. S9: Results on the low-light concealed object segmentation task.

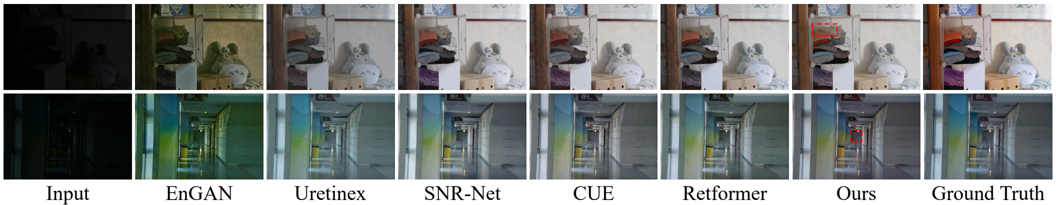

Fig. S10: Failure cases. Our results show blurred texture details in the dashed boxes.

attempts to merge them. This behavior contrasts with the successful separation of the lower clothing, which exhibits more apparent differences. A similar issue is observed in the second image. This limitation is not attributable to the Retinex priors or the RGformer, as neither is specifically designed to highlight subtle differences. To address this challenge, future research could explore extracting texture priors from alternative domains, such as the frequency domain. Such priors could complement those in the RGB domain by emphasizing subtle distinctions. Additionally, inspired by (Lin et al., 2024; Sahoo et al., 2024), we acknowledge that further tuning the noise variance parameters could enhance the latent diffusion model's capacity to address noise across varying levels and facilitate the generation of higher-quality enhanced images. In future work, we plan to thoroughly investigate how this strategy can contribute to the development of a more effective IDIR algorithm.

References

Diederik P Kingma and Max Welling. Auto-encoding variational bayes. *arXiv preprint arXiv:1312.6114*, 2013. 1

Shanchuan Lin, Bingchen Liu, Jiashi Li, and Xiao Yang. Common diffusion noise schedules and sample steps are flawed. In *WACV*, pp. 5404–5411, 2024. 5

Subham Sekhar Sahoo, Aaron Gokaslan, Chris De Sa, and Volodymyr Kuleshov. Diffusion models with learned adaptive noise. *NeurIPS*, 2024. 5

Bin Xia, Yulun Zhang, Shiyin Wang, Yitong Wang, Xinglong Wu, Yapeng Tian, Wenming Yang, and Luc Van Gool. Diffir: Efficient diffusion model for image restoration. In *ICCV*, 2023. 1